nanomaterials

MDPI

Article

Asymmetric Interfaces in Epitaxial Off-Stoichiometric $Fe_{3+x}Si_{1-x}$/Ge/$Fe_{3+x}Si_{1-x}$ Hybrid Structures: Effect on Magnetic and Electric Transport Properties

Anton S. Tarasov [1,2,*], Ivan A. Tarasov [1,*], Ivan A. Yakovlev [1], Mikhail V. Rautskii [1], Ilya A. Bondarev [1,3], Anna V. Lukyanenko [1,2], Mikhail S. Platunov [1,4], Mikhail N. Volochaev [1,5], Dmitriy D. Efimov [6], Aleksandr Yu. Goikhman [6], Boris A. Belyaev [1,2], Filipp A. Baron [1], Lev V. Shanidze [1,3], Michael Farle [1,7], Sergey N. Varnakov [1], Sergei G. Ovchinnikov [1,2] and Nikita V. Volkov [1,2]

1 Kirensky Institute of Physics, Federal Research Center KSC SB RAS, 660036 Krasnoyarsk, Russia; yia@iph.krasn.ru (I.A.Y.); rmv@iph.krasn.ru (M.V.R.); iabond@iph.krasn.ru (I.A.B.); lav@iph.krasn.ru (A.V.L.); platunov@iph.krasn.ru (M.S.P.); volochaev91@mail.ru (M.N.V.); belyaev@iph.krasn.ru (B.A.B.); spintron@hotmail.com (F.A.B.); shanidze.l.v@mail.ru (L.V.S.); michael.farle@uni-due.de (M.F.); vsn@iph.krasn.ru (S.N.V.); sgo@iph.krasn.ru (S.G.O.); volk@iph.krasn.ru (N.V.V.)
2 Institute of Engineering Physics and Radio Electronics, Siberian Federal University, 660041 Krasnoyarsk, Russia
3 Krasnoyarsk Scientific Center, Federal Research Center KSC SB RAS, 660036 Krasnoyarsk, Russia
4 Synchrotron Radiation Facility SKIF, Boreskov Institute of Catalysis SB RAS, Nikol'skiy Prospekt 1, 630559 Kol'tsovo, Russia
5 REC Smart Materials and Biomedical Applications, Immanuel Kant Baltic Federal University, 236041 Kaliningrad, Russia
6 REC Functional Nanomaterials, Immanuel Kant Baltic Federal University, 236016 Kaliningrad, Russia; granitny.kot@gmail.com (D.D.E.); aygoikhman@gmail.com (A.Y.G.)
7 Faculty of Physics and Center for Nanointegration (CENIDE), University of Duisburg-Essen, 47057 Duisburg, Germany
* Correspondence: taras@iph.krasn.ru (A.S.T.); tia@iph.krasn.ru (I.A.T.)

Abstract: Three-layer iron-rich $Fe_{3+x}Si_{1-x}$/Ge/$Fe_{3+x}Si_{1-x}$ ($0.2 < x < 0.64$) heterostructures on a Si(111) surface with Ge thicknesses of 4 nm and 7 nm were grown by molecular beam epitaxy. Systematic studies of the structural and morphological properties of the synthesized samples have shown that an increase in the Ge thickness causes a prolonged atomic diffusion through the interfaces, which significantly increases the lattice misfits in the Ge/$Fe_{3+x}Si_{1-x}$ heterosystem due to the incorporation of Ge atoms into the $Fe_{3+x}Si_{1-x}$ bottom layer. The resultant lowering of the total free energy caused by the development of the surface roughness results in a transition from an epitaxial to a polycrystalline growth of the upper $Fe_{3+x}Si_{1-x}$. The average lattice distortion and residual stress of the upper $Fe_{3+x}Si_{1-x}$ were determined by electron diffraction and theoretical calculations to be equivalent to 0.2 GPa for the upper epitaxial layer with a volume misfit of −0.63% compared with a undistorted counterpart. The volume misfit follows the resultant interatomic misfit of |0.42|% with the bottom Ge layer, independently determined by atomic force microscopy. The variation in structural order and morphology significantly changes the magnetic properties of the upper $Fe_{3+x}Si_{1-x}$ layer and leads to a subtle effect on the transport properties of the Ge layer. Both hysteresis loops and FMR spectra differ for the structures with 4 nm and 7 nm Ge layers. The FMR spectra exhibit two distinct absorption lines corresponding to two layers of ferromagnetic $Fe_{3+x}Si_{1-x}$ films. At the same time, a third FMR line appears in the sample with the thicker Ge. The angular dependences of the resonance field of the FMR spectra measured in the plane of the film have a pronounced easy-axis type anisotropy, as well as an anisotropy corresponding to the cubic crystal symmetry of $Fe_{3+x}Si_{1-x}$, which implies the epitaxial orientation relationship of $Fe_{3+x}Si_{1-x}$ (111)[0−11] || Ge(111)[1−10] || $Fe_{3+x}Si_{1-x}$ (111)[0−11] || Si(111)[1−10]. Calculated from ferromagnetic resonance (FMR) data saturation magnetization exceeds 1000 kA/m. The temperature dependence of the electrical resistivity of a Ge layer with thicknesses of 4 nm and 7 nm is of semiconducting type, which is, however, determined by different transport mechanisms.

check for updates

Citation: Tarasov, A.S.; Tarasov, I.A.; Yakovlev, I.A.; Rautskii, M.V.; Bondarev, I.A.; Lukyanenko, A.V.; Platunov, M.S.; Volochaev, M.N.; Efimov, D.D.; Goikhman, A.Y.; et al. Asymmetric Interfaces in Epitaxial Off-Stoichiometric $Fe_{3+x}Si_{1-x}$/Ge/$Fe_{3+x}Si_{1-x}$ Hybrid Structures: Effect on Magnetic and Electric Transport Properties. *Nanomaterials* **2022**, *12*, 131. https://doi.org/10.3390/nano12010131

Academic Editor: Vasileios Tzitzios

Received: 1 December 2021
Accepted: 26 December 2021
Published: 31 December 2021

Publisher's Note: MDPI stays neutral with regard to jurisdictional claims in published maps and institutional affiliations.

Keywords: iron silicide; germanium; molecular beam epitaxy; epitaxial stress; lattice distortion; dislocation lattices; FMR; Rutherford backscattering; spintronics

1. Introduction

Spintronic devices, which have already found their application in such uses as tunnel magnetoresistive elements of hard disk read heads and random magnetic access memory cells [1], are usually based on vertical magnetic tunnel junctions, while semiconductor spintronics [2,3] more often use planar geometry. Vertical three-layer hybrid ferromagnet (FM)/semiconductor (SC)/FM structures combine both approaches and can be promising for both vertical and planar semiconductor spintronics devices [4,5]. Still, great attention of researchers is paid to Heusler alloys [6–10] due to their high spin polarization of conduction electrons, such as $Fe_{3+x}Si_{1-x}$, Co_2FeSi, Fe_2MnSi, and Co_2FeAl. They have a cubic crystal structure and can be relatively easily grown on standard semiconductor substrates such as Si [11], Ge [12], GaAs [13]. The use of Ge on the other hand looks very attractive from a technological point of view, since it requires lower growth temperatures than Si while remaining compatible with CMOS technologies [14,15].

Furthermore, Ge is fundamentally more promising than Si, since it has a higher electron and hole mobility and a higher spin–orbit interaction, which can control spin-dependent transport by an electric field [16,17]. Thus, the creation of spintronic devices and the subsequent implementation of spin functionality, multilayer hybrid structures with controlled magnetic and transport properties are essential to building MOSFET-type devices based on vertically stacked FM/Ge/FM structures. All this requires systematic technological and fundamental research.

The consecutive growth of multilayer epitaxial structures consisting of materials such as the semiconducting Ge and FM Fe_3Si is a nontrivial technological problem due to the different growth temperatures of the layers [18,19]. An elevated growth temperature of the Ge layer results in an increased Ge diffusion into the silicide bottom layer and also the diffusion of Fe into the substrate and Si atoms in the opposite direction. The reduction of the Ge diffusion and two-dimensional stable epitaxial growth of Ge films on the Fe_3Si surface up to a thickness of dozens of nanometres is achieved via the formation of diffusion barriers and terminating the Fe_3Si surface with several monolayers of silicon [11,18,20]. In turn, the tuning of the electronic and magnetic properties of the $Fe_{3+x}Si_{1-x}$ compounds may be accomplished by changing chemical and structural order and composition [21,22] that inevitably changes the landscape of the epitaxial formation of the $Fe_{3+x}Si_{1-x}$/Ge/$Fe_{3+x}Si_{1-x}$ heterostructures.

Here, we study the formation of vertical three-layer $Fe_{3+x}Si_{1-x}$/Ge/$Fe_{3+x}Si_{1-x}$ heterostructures on a Si(111) substrate. The effect of crystal quality on structural, morphological, magnetic, and transport properties and of the thickness of individual Ge layers on magnetic anisotropy and the temperature behaviour of the electrical resistance is investigated.

2. Sample Synthesis and Experimental Details

Two samples (#6 and #7) were synthesized, which are three-layer structures $Fe_{3+x}Si_{1-x}$/Ge/$Fe_{3+x}Si_{1-x}$ with a thickness of germanium d_{Ge} = 4 nm and 7 nm. Iron silicide $Fe_{3+x}Si_{1-x}$ layers were grown by the molecular beam epitaxy. Iron and silicon were co-deposited from different sources in an atomic ratio close to 3:1 but enriched with iron. Knudsen cells with indirect thermal heating of the crucible are used as sources. During the synthesis of the silicide layers, the substrate temperature was maintained at 150 °C. The deposition time was chosen so that the thickness of the $Fe_{3+x}Si_{1-x}$ layers was about 7–10 nm. A semi-insulating n-type Si(111) silicon wafer with a resistivity ρ = 3000–7000 Ohm·cm (phosphorus concentration $n \approx 1 \times 10^{12}$ 1/cm^3) was used as a substrate to minimize a Si contribution to the electric transport in a three-layer structure. Before loading into a high-vacuum (UHV)

chamber, substrates were cleaned in a solution of H_2O_2:NH_4OH:H_2O in a 1:1:1 ratio and a 5% solution of hydrofluoric acid HF, followed by thermal annealing at a temperature of 900 °C under UHV conditions (for details see [23]). As a result, we obtain the well-known Si(111) 7 × 7 surface reconstruction. The substrate was kept at 150 °C for 30 min during the growth of the $Fe_{3+x}Si_{1-x}$ film. The entire synthesis process was controlled in situ using reflected high-energy electron diffraction (RHEED). The diffraction data (Figure 1b) shows the first $Fe_{3+x}Si_{1-x}$ layer on Si(111) 7 × 7 was formed epitaxially and has a single-crystal structure.

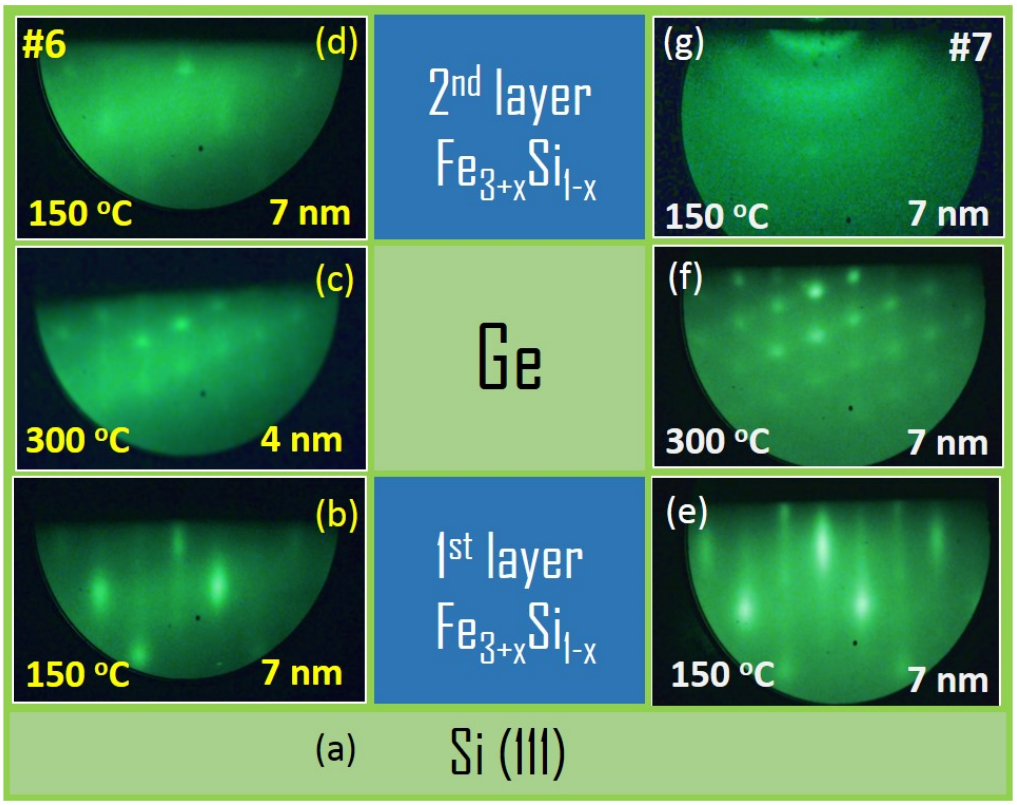

Figure 1. (**a**) Middle panel shows the schematics of the three-layer structure $Fe_{3+x}Si_{1-x}$/Ge/$Fe_{3+x}Si_{1-x}$/Si(111). The panels on the left and right show the respective RHEED patterns obtained after deposition of the respective layer for samples #6 and #7: (**b**)—1st $Fe_{3+x}Si_{1-x}$, (**c**)—Ge 4 nm, (**d**)—2nd $Fe_{3+x}Si_{1-x}$ and (**e**)—1st $Fe_{3+x}Si_{1-x}$, (**f**)—Ge 7 nm, and (**g**)—2nd $Fe_{3+x}Si_{1-x}$, respectively.

After the first layer of the silicide was grown, the sample temperature was raised to 300 °C for 10 min. Then 3–5 nm Ge was deposited. According to the RHEED data (Figure 1c), the germanium layer also has an epitaxial, single-crystal structure. After the deposition of germanium, the substrate temperature was reduced to 150 °C for 10 min and the second silicide layer was deposited. The RHEED pattern is characterised by the A2 (Strukturbericht [23]) in <110> direction. The observed diffraction suggests that the second silicide layer was formed epitaxially and has a single-crystal structure identical to the first layer. In sample #7, the Ge thickness is a factor two larger than in #6. As a result, the RHEED pattern from the Ge layer (Figure 1f) did not change and even became slightly more pronounced compared with the thinner layer on sample #6 (Figure 1c). Despite this, the diffraction pattern for the 2nd $Fe_{3+x}Si_{1-x}$ layer of sample #7 contains only reflections in the form of diffuse Debye rings. This geometry of the diffraction pattern indicates the formation of a nanocrystalline or polycrystalline structure. RHEED patterns are satisfactorily described with the $Fe_{3+x}Si_{1-x}(111)[0-11]$ || $Ge(111)[1-10]$ || $Fe_{3+x}Si_{1-x}(111)[0-11]$ || $Si(111)[1-10]$ orientation relationships (OR). These results were obtained directly in the UHV chamber.

The microstructure of the samples was studied using atomic force (AFM) and transmission electron (TEM) microscopy. The surface morphology of the films was measured using AFM in a semicontact scanning mode (DPN 5000 device, NanoInk, Skokie, IL, USA) using probes with a curvature radius of ~6 nm (CSG30, NT-MDT SI, Moscow, Russia). AFM data processing and statistical analysis of images were carried out using the free software Gwyddion (version 2.51) and an image processing package Fiji [24]. Depth distribution of Fe, Si, and Ge of the epitaxial $Fe_{1-x}Si_x$ alloy films were studied with Rutherford backscattering spectroscopy (RBS) at the accelerator HVEE AN-2500 (6REC Functional Nanomaterials, Immanuel Kant Baltic Federal University, Kaliningrad, Russia). The films' cross-sections and plan view TEM lamella were made using a focused ion beam (FIB) FB-2100 (Hitachi, Tokyo, Japan) setup for electron microscopic investigations. Static and dynamic magnetic properties were investigated using Lakeshore's 8600 Series vibration sample magnetometer (VSM) and Bruker's ELEXSYS-E580 electron paramagnetic resonance (EPR) spectrometer (Krasnoyarsk Territorial Shared Resource Center, Krasnoyarsk Scientific Center, Russian Academy of Sciences). Resistivity and current–voltage characteristics were measured using a Keithley 2634b SourceMeter precision multimeter over a temperature range of 4.2 K to 300 K in a home-built helium flow cryostat [25].

3. Results and Discussion

3.1. Structural Properties

3.1.1. Analysis of Epitaxial Orientation Relationships

In the TEM images (Figure 2) one can identify three separate layers between the Si(111) substrate and the protective layer. The thickness of each layer is 7 nm for the $Fe_{3+x}Si_{1-x}$ layers of both samples and 4 nm and 7 nm for the Ge layers of samples #6 and #7, respectively. It should be noted that in the case of sample #6 (Figure 2a,b), the brightness of the upper and lower $Fe_{3+x}Si_{1-x}$ layers is noticeably different, which is mainly caused by "diffraction contrast" [26] due to the Bragg scattering at crystallographic orientations and different electron density (mass of constituent elements) and different thickness of the specimen. In the dark field mode, the higher the Z value and the density of the material are, the darker the image is. From the diffraction pattern of the silicide layers (Figure 2c) we conclude that the $Fe_{3+x}Si_{1-x}$ epilayers have the same orientation relationship $Fe_{3+x}Si_{1-x}(111)[0{-}11]$ || $Ge(111)[1{-}10]$ || $Fe_{3+x}Si_{1-x}(111)[0{-}11]$ with the silicon substrate $Si(111)[1{-}10]$ and the formation of a chemically disordered bcc-type $Fe_{3+x}Si_{1-x}$ alloy. The superstructure reflections of a chemically ordered alloy, i.e., (111, −111), are absent. In turn, the polycrystalline nature of the upper layer of sample #7 is supported by electron diffraction measured along the [−110] and [1−21] zone axis of Si. The OR derived for them are $Fe_{3+x}Si_{1-x}(110)[001]{-}8.5°$ || $Si(111)[-110]$ and $Fe_{3+x}Si_{1-x}(0{-}11)[0{-}11]{-}8.5°$ || $Si(111)[1{-}21]$, which indicate differently orientated crystallites (Figure 3 (Sample #7)).

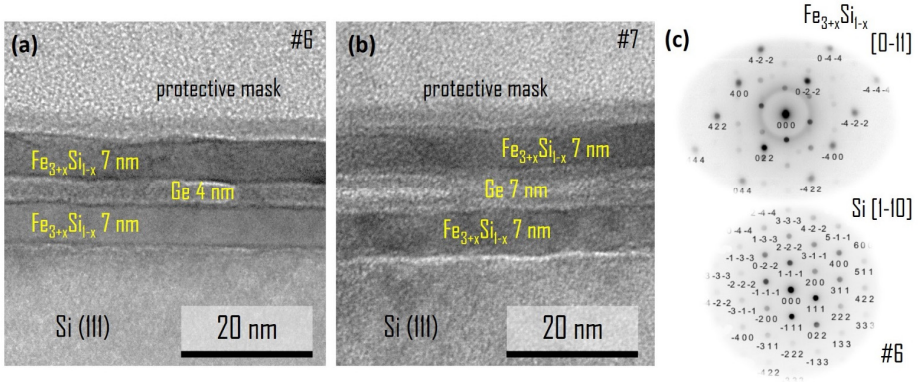

Figure 2. TEM images of cross section of $Fe_{3+x}Si_{1-x}$/Ge/$Fe_{3+x}Si_{1-x}$/Si(111) samples #6 (**a**) and #7 (**b**). Unit cell and crystallographic plane with iron atoms of the $Fe_{3+x}Si_{1-x}$ epilayer in the (111) film plane (**c**).

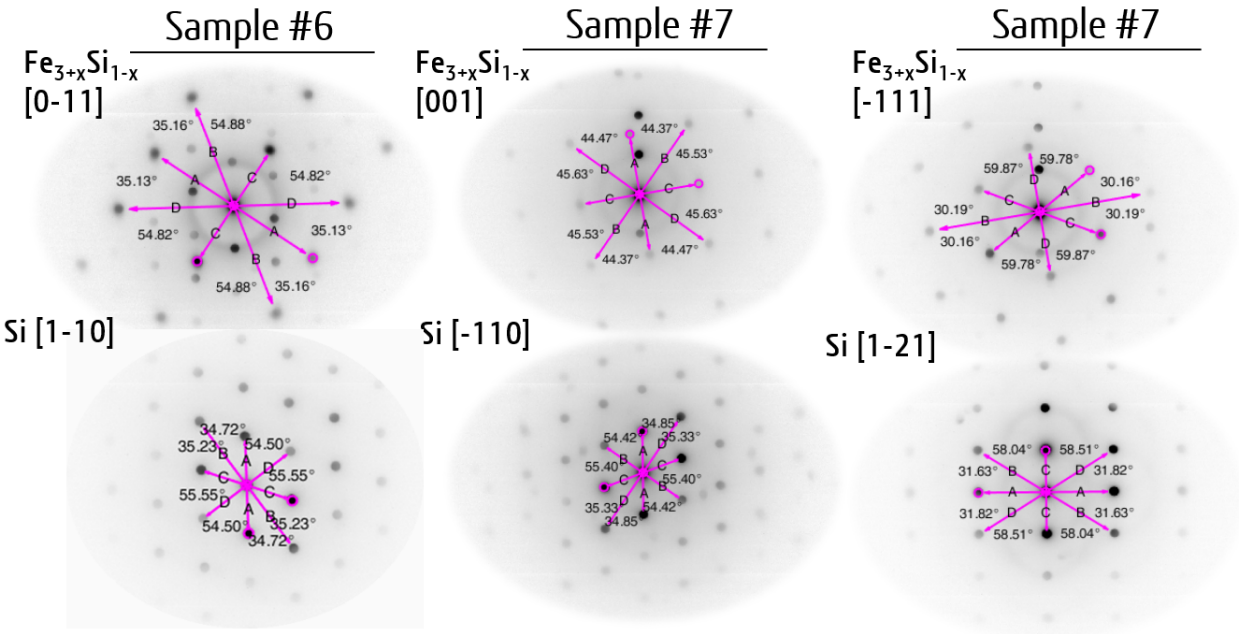

Figure 3. TEM electron diffraction pattern of cross-section of $Fe_{3+x}Si_{1-x}$/Ge/$Fe_{3+x}Si_{1-x}$/Si(111) samples #6 and #7 along different projections (zone axes). The angles of reciprocal lattice vectors are given for each phase.

We also analysed the epitaxial stress in the epilayer and in the crystallites of the polycrystalline layer of the Fe-Si alloy. Changing the chemical composition within the trilayers based on ferromagnetic $Fe_x(Si_{1-y}Ge_y)$ alloys can be used to tune the epitaxial stress and thereby the electronic structure and, as a result, the functional properties of the material [27–29].

The lattice distortions $\delta_{a,b,c}$ and $\delta_{\alpha,\beta,\gamma}$ can be regarded as additives to a, b, c and α, β, γ parameters and in the most cases result in the change of crystal symmetry [30]. By measuring interplanar distances with the X-ray diffraction (XRD) method or TEM in principle, one can determine the lattice distortions solving a given system of equations relating the interplanar distances and the lattice parameters [30]. Except for interplanar distance, TEM allows one to derive the distribution of the angular distances between the planes forming the diffraction pattern [31]. For a low-symmetry crystal system, the equations become cumbersome and, in some cases, suggesting minimal distortion may be simplified to linear forms [32]. In general, they require the application of numerical methods of solving nonlinear and transcendental systems of equations.

For the epitaxial layer of the iron–silicon alloy, we consider two representations of the crystal lattice, a cubic one and a hexagonal one. The Fe_3Si silicide belongs to the *Fm-3m* group symmetry, and it has DO3 structure (Strukturbericht). The *Im-3m* group is used for chemically disordered alloy (A2). According to the interpretation of the diffraction pattern [31], the epi-layer has the following OR: $Fe_{3+x}Si_{1-x}(111)$ [0−11] || Si(111) [1−10]. The strain [33] is 3.54%, and the area misfit is −8.35% for this epitaxial OR. Thus, the c lattice parameter is under the same compressive stress while the a and b parameters are slightly relaxed. The hexagonal symmetry of the Si(111) surface can cause an isotropic stress for the α, β, γ angles. However, other combinations of the angles and a, b, c distortions are possible and are discussed below. The second representation is that the hexagonal symmetry of the (111) plane allows one to use the Fe_3Si lattice with the P3 space group, where a, b correspond to [0 −0.5 0.5] and [0.5 0 0.5] directions and c is [111] in the cubic lattice of the Fe_3Si. In this case, the lattice parameters are a, b = 0.3997 and c = 0.979 nm (c/a = 2.449) for Fe_3Si composition [34].

The fit of the experimental set of the interplanar distances without consideration of lattice distortions yields the following lattice parameters of sample #6 for the cubic represen-

tation, a, b, c = 0.56801 nm, for the hexagonal one a, b, = 0.348 nm and c = 1.138 nm, which closely corresponds to the $Fe_{80}Si_{20}$ alloy [35]. In turn, the diffraction patterns of sample #7 correspond to a, b, c = 0.57137 nm (zone axis $Fe_{3+x}Si_{1-x}$ [1]) and a, b, c = 0.56994 nm (zone axis $Fe_{3+x}Si_{1-x}$ [−111]). The corresponding chemical compositions are $Fe_{91}Si_9$ and $Fe_{86}Si_{14}$, respectively. The calibration was carried out based on the diffraction pattern of the silicon substrate (Figure 3) with a = 0.54307 nm by fitting with the RANSAC lattice procedure [31]. As shown in Figure 4, the lattice parameter a changes in the 0.559–0.582 nm range in ternary Fe–Ge–Si alloys. These indirectly determined lattice parameters indicate that the $Fe_{3+x}Si_{1-x}$ silicide in sample #7 may contain the germanium atoms uniformly distributed over the $Fe_{3+x}Si_{1-x}$ silicide. In the case of equal silicon content, with close to 25 at.% co-deposited, the lattice parameter of the $Fe_{3+x}Si_{1-x}$ increases due to the incorporation of Ge atoms (Figure 4). The hexagonal one shows the a, b lattice constants under a large compressive strain with a value even less than the one corresponding to Si (0.384 nm), which indirectly confirms that the lattice distortion of the epilayer should be taken into account.

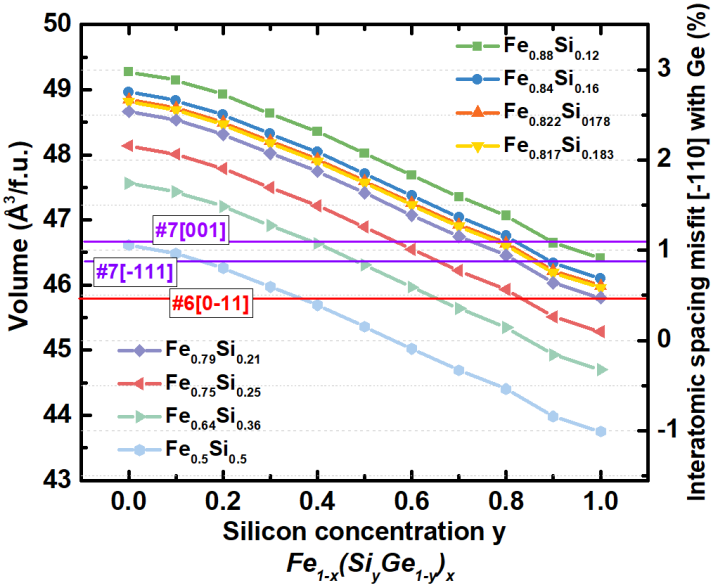

Figure 4. Dependence of unit cell volume per functional unit of ternary Fe–Ge–Si alloys.

3.1.2. Estimation of Lattice Distortions

To estimate the lattice distortions, we applied a numerical approach assuming a uniformly distributed array of random initial parameters for different configurations of the epitaxial strain. The algorithm consists of several steps restricting the range of solutions. The first step iteratively narrows the solution range based on the function $F = \sum_{i=1}^{n} f_i(\delta_{a,b,c,\alpha,\beta,\gamma}) - P_i$ relating the known experimental values of P_i (d-spacing and angles between crystallographic planes observed in the diffraction pattern) by limiting each iteration to $F < 0.2$ from the uniformly distributed array of random initial parameters (2×10^5 solution combinations). n is the total number of experimental values; the function f relates the d-spacings and angles between crystallographic planes to the unit cell parameters [30]. The procedure repeats 2×10^3 times then the restricted solution range is defined by the median of the lowest and highest values of lower and upper boundaries. The second step consists of the division of the solution range by the solutions found according to the range $\delta_{a,b,c,\alpha,\beta,\gamma}$ values. It is divided into positive and negative ranges. Then, the range is again narrowed with the help of the hybrid approach of simulated annealing (SA) algorithm [36] and post-minimisation by the Nelder–Mead simplex algorithm [37]. For each SA procedure, the initial parameter used was taken from the uniformly distributed array of distortion parameters within the restricted range, in a total of 10^6 sets. The final

step generates a uniformly distributed array of random initial parameters (10^7 solution sets) within the set of previously restricted sets. It limits the solutions resulting in the 200 most minimal values of the residual function defined as standard deviation from the set of experimental values P_i.

To verify the applicability of the algorithm, we considered the following lattice distortion configuration, $\delta_{a,b} = -0.001991$, $\delta_c = 0.042908$ nm, $\delta_{\alpha,\beta} = -0.07512^\circ$, and $\delta_\gamma = 0.12^\circ$, for a cubic lattice by solving the direct problem and by applying our numerical approach to estimate the lattice distortions. This comparison allows to estimate the set of possible solutions within an experimental error. It can be seen from Table 1 that two solutions were found. The one that corresponds to the true values shows the minor residual function (the standard deviation from the set of experimental values). It is also noticeable that the standard deviation from the average value of the stress parameters is several times less for the solution close to the true values, which indicate more narrow solution zones and can serve as a criterion to estimate the validity of one solution among others.

Table 1. Comparison of the true values of lattice distortions of a cubic lattice with the numerical solution found for two types of calculations $\delta_a = \delta_b \neq \delta_c$, $\delta_\alpha = \delta_\beta \neq \delta_\gamma$. The sign of $\pm$ indicates the standard deviation from the average value of the 200 solutions with the minimal residual function observed.

	Residual	**$\delta_{a,b}$, nm**	**δ_c, nm**	**$\delta_{\alpha,\beta}$, deg.**	**δ_γ, deg.**
True values of quantities		$\mathbf{-1.991 \times 10^{-3}}$	$\mathbf{4.2908 \times 10^{-2}}$	**−0.07512**	**0.12**
Solutions	$2.13 \times 10^{-10} \pm 6.44 \times 10^{-11}$	$-1.991 \times 10^{-3} \pm 5.99 \times 10^{-8}$	$4.279 \times 10^{-2} \pm 1.69 \times 10^{-5}$	-0.07629 ± 0.0017	0.1212 ± 0.0017
	$9.34 \times 10^{-10} \pm 2.48 \times 10^{-10}$	$-1.991 \times 10^{-3} \pm 2.31 \times 10^{-7}$	$6.205 \times 10^{-2} \pm 7.46 \times 10^{-5}$	0.114 ± 0.0074	-0.0668 ± 0.0072

Several possible solutions for the three epitaxial patterns (Figure 4) are given in Table 2. For the all-epitaxial trilayer sample #6, four configurations of the distortions were considered (listed in Table 2). As can be seen, the number of possible solutions increases while relaxing the strain configuration. It is worth mentioning that the configuration with the isotropic $\delta_{\alpha,\beta,\gamma}$ strain shows the most prominent residual function and a different δ_a value in comparison with others consistent with $\delta_a = -0.001368$ nm. One may conclude that the better convergence is observed for two distortion configurations which are (i) $\delta_a \neq \delta_b = \delta_c$, $\delta_\alpha = 0$, $\delta_\beta \neq \delta_\gamma$; (ii) $\delta_a \neq \delta_b = \delta_c$, $\delta_\alpha \neq \delta_\beta \neq \delta_\gamma$ (highlighted with green Table 2). It is also seen that the solution with $-\delta_\beta$, δ_γ and $-\delta_\beta$, δ_γ are equivalent. Thus, the lattice parameters of the $Fe_{3+x}Si_{1-x}$ epilayer (hexagonal representation) are a, b, = 0.4019 (0.9844) nm and c = 0.9848 (0.402043) nm after applying the distortion determined, and in the nondistorted case we find c/a = 2.450. The parameter a equals 0.568375 (0.568574) nm for the cubic representation corresponding to 19.06 and 18.37 at.% of silicon. Lattice strain for a given $Fe_{3+x}Si_{1-x}(111)[0-11]$ habit plane is 0.16%; the lattice is under compressive strain since the volume misfit between the estimated undistorted and lattices is −0.63%. In the case of sample #7 (zone axis [001]), it is not possible to assess the distortion of the c lattice constant. It was determined that the a and b parameters are slightly distorted while δ_γ reaches −1.17 degrees (highlighted with green colour), with the volume misfit with the undistorted counterpart equal to −0.0369%.

Table 2. Solutions for lattice distortions for the $Fe_{3+x}Si_{1-x}$ epilayer of sample #6 and two crystallites of sample #7. Configurations of crystal lattice distortions are given in the table. The sign of ± indicates the standard deviation from the average value of the 200 solutions with the minimal residual function observed.

		Residual	δ_a, nm	δ_b, nm	δ_c, nm	δ_α, deg.	δ_β, deg.	δ_γ, deg.
				Sample #6 cubic				
Solutions found	$\delta_a \neq \delta_b = \delta_c, \delta_\alpha = \delta_\beta = \delta_\gamma$	$1.11 \times 10^{-6} \pm 1.31 \times 10^{-16}$ $1.11 \times 10^{-6} \pm 6.11 \times 10^{-12}$ $1.18 \times 10^{-6} \pm 4.67 \times 10^{-11}$	$-1.199 \times 10^{-3} \pm 2.55 \times 10^{-11}$ $-1.200 \times 10^{-3} \pm 3.66 \times 10^{-7}$ $-1.148 \times 10^{-3} \pm 1.34 \times 10^{-6}$	$2.657 \times 10^{-3} \pm 1.29 \times 10^{-13}$ $2.655 \times 10^{-3} \pm 6.14 \times 10^{-9}$ $2.656 \times 10^{-3} \pm 3.31 \times 10^{-8}$			$-0.0165 \pm 2.15 \times 10^{-9}$ $-0.0173 \pm 1.17 \times 10^{-5}$ $8.181 \times 10^{-4} \pm 5.72 \times 10^{-6}$	
	$\delta_a \neq \delta_b = \delta_c, \delta_\alpha = 0;$ $\delta_\beta \neq \delta_\gamma$	$1.50 \times 10^{-8} \pm 7.49 \times 10^{-14}$	$-1.368 \times 10^{-3} \pm 1.82 \times 10^{-10}$	$1.00 \times 10^{-3} \pm 3.33 \times 10^{-10}$	0		$0.0163 \pm 4.07 \times 10^{-6}$	$0.0208 \pm 4.06 \times 10^{-6}$
		$1.50 \times 10^{-8} \pm 1.25 \times 10^{-13}$	$-1.368 \times 10^{-3} \pm 2.75 \times 10^{-9}$	$1.00 \times 10^{-3} \pm 3.49 \times 10^{-9}$	0		$-0.0442 \pm 2.26 \times 10^{-6}$	$0.0814 \pm 2.17 \times 10^{-6}$
		$1.50 \times 10^{-8} \pm 3.62 \times 10^{-14}$	$-1.368 \times 10^{-3} \pm 4.39 \times 10^{-11}$	$1.00 \times 10^{-3} \pm 7.15 \times 10^{-11}$	0		$0.0605 \pm 2.87 \times 10^{-6}$	$-0.0234 \pm 2.88 \times 10^{-6}$
		$1.50 \times 10^{-8} \pm 8.83 \times 10^{-14}$	$-1.368 \times 10^{-3} \pm 9.75 \times 10^{-10}$	$1.00 \times 10^{-3} \pm 3.00 \times 10^{-9}$	0		$0.0794 \pm 1.00 \times 10^{-5}$	$-0.0422 \pm 1.01 \times 10^{-5}$
		$1.50 \times 10^{-8} \pm 8.22 \times 10^{-14}$	$-1.368 \times 10^{-3} \pm 1.22 \times 10^{-10}$	$1.00 \times 10^{-3} \pm 1.35 \times 10^{-10}$	0		$0.0255 \pm 8.56 \times 10^{-6}$	$0.0627 \pm 8.57 \times 10^{-6}$
	$\delta_a \neq \delta_b = \delta_c, \delta_\alpha \neq \delta_\beta = -\delta_\gamma$	$6.49 \times 10^{-7} \pm 4.54 \times 10^{-17}$	$-1.341 \times 10^{-3} \pm 4.77 \times 10^{-10}$	$-2.27 \times 10^{-6} \pm 1.45 \times 10^{-14}$	$-0.175 \pm 2.71 \times 10^{-12}$		$0.0003 \pm 6.71 \times 10^{-4}$	$-0.0003 \pm 6.71 \times 10^{-4}$
		$3.54 \times 10^{-7} \pm 8.57 \times 10^{-19}$	$-1.368 \times 10^{-3} \pm 1.20 \times 10^{-11}$	$1.20 \times 10^{-3} \pm 1.05 \times 10^{-7}$	$0.032 \pm 2.12 \times 10^{-5}$		$0.0002 \pm 4.51 \times 10^{-6}$	$-0.0002 \pm 4.51 \times 10^{-6}$
		$3.54 \times 10^{-7} \pm 4.98 \times 10^{-18}$	$-1.368 \times 10^{-3} \pm 5.72 \times 10^{-10}$	$5.95 \times 10^{-4} \pm 2.86 \times 10^{-7}$	$-0.085 \pm 5.80 \times 10^{-5}$		$0.0002 \pm 2.52 \times 10^{-6}$	$-0.0002 \pm 2.52 \times 10^{-6}$
		$3.54 \times 10^{-7} \pm 5.47 \times 10^{-19}$	$-1.368 \times 10^{-3} \pm 2.25 \times 10^{-12}$	$1.44 \times 10^{-3} \pm 3.47 \times 10^{-8}$	$0.085 \pm 6.96 \times 10^{-6}$		$0.0002 \pm 3.65 \times 10^{-7}$	$-0.0002 \pm 3.65 \times 10^{-7}$
		$3.54 \times 10^{-7} \pm 2.82 \times 10^{-20}$	$-1.367 \times 10^{-3} \pm 2.86 \times 10^{-10}$	$1.00 \times 10^{-3} \pm 3.79 \times 10^{-8}$	$0.001 \pm 7.64 \times 10^{-6}$		$-0.087 \pm 9.32 \times 10^{-6}$	$0.087 \pm 9.32 \times 10^{-6}$
		$3.54 \times 10^{-7} \pm 3.92 \times 10^{-20}$	$-1.367 \times 10^{-3} \pm 2.76 \times 10^{-10}$	$1.00 \times 10^{-3} \pm 4.07 \times 10^{-8}$	$0.001 \pm 8.20 \times 10^{-6}$		$0.087 \pm 9.14 \times 10^{-6}$	$-0.087 \pm 9.14 \times 10^{-6}$
	$\delta_a \neq \delta_b = \delta_c, \delta_\alpha \neq \delta_\beta \neq \delta_\gamma$	$1.07 \times 10^{-6} \pm 8.82 \times 10^{-12}$	$-1.341 \times 10^{-3} \pm 1.33 \times 10^{-7}$	$-7.99 \times 10^{-8} \pm 2.46 \times 10^{-9}$	$-0.145 \pm 4.93 \times 10^{-7}$		$0.012 \pm 3.10 \times 10^{-4}$	$0.024 \pm 3.21 \times 10^{-4}$
		$1.50 \times 10^{-8} \pm 8.84 \times 10^{-15}$	$-1.368 \times 10^{-3} \pm 2.12 \times 10^{-9}$	$1.10 \times 10^{-3} \pm 1.39 \times 10^{-6}$	$0.018 \pm 2.80 \times 10^{-4}$		$0.012 \pm 1.78 \times 10^{-4}$	$0.025 \pm 1.78 \times 10^{-4}$
		$1.50 \times 10^{-8} \pm 4.83 \times 10^{-15}$	$-1.368 \times 10^{-3} \pm 3.57 \times 10^{-9}$	$6.69 \times 10^{-4} \pm 5.75 \times 10^{-7}$	$-0.070 \pm 1.15 \times 10^{-4}$		$0.012 \pm 8.63 \times 10^{-5}$	$0.026 \pm 8.63 \times 10^{-5}$
		$1.50 \times 10^{-8} \pm 3.30 \times 10^{-15}$	$-1.368 \times 10^{-3} \pm 2.58 \times 10^{-9}$	$1.37 \times 10^{-3} \pm 4.99 \times 10^{-7}$	$0.071 \pm 1.00 \times 10^{-4}$		$0.012 \pm 1.014 \times 10^{-4}$	$0.025 \pm 1.012 \times 10^{-4}$
		$1.50 \times 10^{-8} \pm 3.02 \times 10^{-14}$	$-1.368 \times 10^{-3} \pm 6.76 \times 10^{-9}$	$1.01 \times 10^{-3} \pm 3.04 \times 10^{-6}$	$-0.001 \pm 6.13 \times 10^{-4}$		$-0.060 \pm 1.87 \times 10^{-4}$	$0.097 \pm 1.87 \times 10^{-4}$
		$1.50 \times 10^{-8} \pm 8.20 \times 10^{-15}$	$-1.368 \times 10^{-3} \pm 2.26 \times 10^{-9}$	$1.02 \times 10^{-3} \pm 1.12 \times 10^{-5}$	$0.001 \pm 2.26 \times 10^{-4}$		$0.070 \pm 1.22 \times 10^{-4}$	$-0.033 \pm 1.23 \times 10^{-4}$
		$1.50 \times 10^{-8} \pm 8.97 \times 10^{-13}$	$-1.368 \times 10^{-3} \pm 1.77 \times 10^{-8}$	$9.94 \times 10^{-4} \pm 1.63 \times 10^{-5}$	$-0.005 \pm 3.3 \times 10^{-3}$		$0.090 \pm 6.70 \times 10^{-4}$	$-0.053 \pm 6.69 \times 10^{-4}$
		$1.50 \times 10^{-8} \pm 1.57 \times 10^{-13}$	$-1.368 \times 10^{-3} \pm 1.10 \times 10^{-8}$	$9.97 \times 10^{-4} \pm 1.25 \times 10^{-5}$	$-0.004 \pm 2.5 \times 10^{-3}$		$-0.048 \pm 4.38 \times 10^{-4}$	$0.085 \pm 4.37 \times 10^{-4}$
				Sample #6 hexagonal				
	$\delta_a = \delta_b \neq \delta_c, \delta_\alpha \neq \delta_\beta \neq \delta_\gamma = 0$	$1.05 \times 10^{-6} \pm 7.75 \times 10^{-16}$	$0.0539 \pm 1.88 \times 10^{-10}$	$-0.1532 \pm 4.84 \times 10^{-11}$	$-4.74 \times 10^{-4} \pm 6.26 \times 10^{-11}$	$0.1439 \pm 3.2 \times 10^{-11}$	0	
		$1.50 \times 10^{-8} \pm 1.51 \times 10^{-12}$	$0.0539 \pm 2.90 \times 10^{-8}$	$-0.1534 \pm 7.37 \times 10^{-8}$	$0.1068 \pm 4 \times 10^{-6}$	$0.1355 \pm 2.25 \times 10^{-6}$	0	
		$2.98 \times 10^{-6} \pm 2.13 \times 10^{-15}$	$0.0538 \pm 1.7 \times 10^{-9}$	$-0.1529 \pm 7.43 \times 10^{-11}$	$0.1217 \pm 1.69 \times 10^{-10}$	$-2.32 \times 10^{-4} \pm 8.47 \times 10^{-11}$	0	
	$\delta a = \delta_b \neq \delta_c, \delta_\alpha = -\delta_\beta \neq \delta_\gamma = 0;$	$2.79 \times 10^{-6} \pm 2.09 \times 10^{-15}$	$0.0538 \pm 8.61 \times 10^{-10}$	$-0.1529 \pm 1.00 \times 10^{-11}$	$-0.1373 \pm 2.43 \times 10^{-10}$	$0.1373 \pm 2.43 \times 10^{-10}$	0	
		$4.43 \times 10^{-6} \pm 1.98 \times 10^{-14}$	$0.0538 \pm 8.64 \times 10^{-9}$	$-0.1529 \pm 1.00 \times 10^{-10}$	$4.57 \times 10^{-4} \pm 1.86 \times 10^{-9}$	$-4.57 \times 10^{-4} \pm 1.86 \times 10^{-9}$	0	
				Sample #7 cubic–zone axis [001]				
	$\delta_a \neq \delta_b, \delta_c = 0, \delta_\alpha = \delta_\beta = 0, \neq \delta_\gamma$	$8.43 \times 10^{-7} \pm 4.45 \times 10^{-14}$	$5.45 \times 10^{-4} \pm 3.17 \times 10^{-11}$	$-4.55 \times 10^{-4} \pm 7.09 \times 10^{-11}$	-	-	-	$-1.177 \pm 8.67 \times 10^{-8}$
		$9.64 \times 10^{-5} \pm 1.39 \times 10^{-7}$ $8.09 \times 10^{-5} \pm 9.11 \times 10^{-8}$	$-1.29 \times 10^{-6} \pm 7.88 \times 10^{-7}$ $3.16 \times 10^{-4} \pm 2.43 \times 10^{-7}$	$-1.83 \times 10^{-4} \pm 3.77 \times 10^{-7}$ $1.64 \times 10^{-6} \pm 5.15 \times 10^{-7}$	- -	- -	- -	$-1.176 \pm 9.71 \times 10^{-6}$ $-1.174 \pm 4.34 \times 10^{-6}$
				Sample #7 cubic–zone axis [−111]				
	$\delta_a \neq \delta_b \neq \delta_c, \delta_\alpha \neq \delta_\beta \neq \delta_\gamma$	$1.79 \times 10^{-5} \pm 6.77 \times 10^{-20}$	$-6.00 \times 10^{-3} \pm 2.60 \times 10^{-18}$	$2.13 \times 10^{-4} \pm 1.897 \times 10^{-19}$	$1.1 \times 10^{-3} \pm 8.67 \times 10^{-19}$	$1.87 \times 10^{-4} \pm 1.89 \times 10^{-19}$	$-0.9996 \pm 4.22 \times 10^{-19}$	$4.9 \times 10^{-4} \pm 1.73 \times 10^{-18}$
		$1.79 \times 10^{-5} \pm 1.29 \times 10^{-10}$	$5.10 \times 10^{-3} \pm 5.79 \times 10^{-5}$	$4.61 \times 10^{-5} \pm 1.31 \times 10^{-4}$	$-1.1 \times 10^{-3} \pm 8.57 \times 10^{-4}$	0.248 ± 0.0923	-0.1129 ± 0.0706	1.1023 ± 0.0545

The case of zone axis [−111] is the most complex to consider since the habit plane of the silicide is not characterized by a low Miller index plane. The distortion configuration was fully relaxed to estimate all six distortion parameters, i.e., $\delta_a \neq \delta_b \neq \delta_c$, $\delta_\alpha \neq \delta_\beta \neq \delta_\gamma$. As a result, a dozen solutions were found with similar values of the residual function F~1.79 × 10^{-5}. Most of them indicate a relatively wide solution zone according to the deviation from the average value with high values of the angles' distortions (a representative one is shown in Table 2 (Sample #7 cubic–zone axis [−111])). However, one solution is characterized by a low deviation (highlighted with green colour), which we consider a distortion close to the true value. This distortion configuration results in the volume misfit of −0.996%. Thus, all cases we considered indicate that the $Fe_{3+x}Si_{1-x}$ silicide is under compressive stress.

To further estimate the reliability of the results for the lattice distortion of the Fe–Si epilayers, the density functional theory (DFT) was applied. To mimic the epitaxial strain possible in $Fe_3Si(111)/Si(111)$, the Fe_3Si hexagonal unit cell with constrained $a = b = 0.384$ nm and $\gamma = 120°$ angle lattice parameters were used. The c, α, and β lattice parameters and atomic positions were allowed to relax. The residual stress was estimated by calculating the stress tensor for the applied lattice distortions determined for the cubic representations of sample #6 [0−11] and #7 [−111] on the optimised off-stoichiometric $Fe_{80}Si_{20}$ and $Fe_{86}Si_{14}$ unit cell. The DFT calculations were carried out with the help of The Quantum Espresso (QE) package [38]. The electronic exchange-correlation energy was selected using the generalized gradient approximation (GGA) of the Perdew–Burke–Ernzerhof (PBE) scheme [39]. To optimize the unit cell geometry the first Brillouin zone in the reciprocal space was sampled on 8 × 8 × 2 and meshes were chosen according to the Monkhorst–Pack scheme. In all calculations, the cutoff energy E_{cutoff} was equal to 30 Ry. The optimisation of the geometry was performed until the maximum values of the forces acting on atoms were less than 10^{-4} Ry/bohr.

The optimized lattice parameters derived from the DFT calculation of the strained hexagonal lattice of Fe_3Si are $c = 0.99353$ nm (c/a = 2.587), $\delta_\alpha = 0.0431°$, $\delta_\beta = -0.0432°$. They are in relative correspondence with the distortion configuration of sample #6 (hexagonal, Table 2). Our calculation of the residual stress reveals that the crystal lattice of $Fe_{3+x}Si_{1-x}$ alloy in both samples is under compressive strain equivalent to 0.21 and 0.91 GPa.

The transition of the upper Fe–Si alloy layer of sample #7 into a polycrystalline morphology is a consequence of different factors. We assume that the dominant one is the interface of the intermediate Ge layer. The RHEED pattern (Figure 1) indicates that the surface of the Ge layer presents 3D islands with a typical size of 1 nm [40]. Such monocrystalline islands should be faceted enough to serve as separated centres for the formation of $Fe_{3+x}Si_{1-x}$ islands so that not only the (111)||(111) interfaces may appear. The second factor is the lattice mismatch of the Fe–Si and Ge layers. The sample #7 should have a more complex interface structure and composition on the lower $Ge/Fe_{3+x}Si_{1-x}$ and $Fe_{3+x}Si_{1-x}/Si$ boundaries due to a two-times more extended exposition at elevated temperature. The Ge diffusion toward the substrate and silicon atoms in the opposite direction changes the composition and, consequently, the lattice parameters of the epilayer. An increased discrepancy in lattice misfits may promote the formation of differently orientated crystallites to relax the higher values of the epitaxial stress.

3.1.3. Characterisation of the Element Depth Distribution

The depth distribution of the Fe and Si, and Ge atoms were determined with Rutherford backscattering spectroscopy using helium ions, He^+, at 1.504 MeV and a scattering angle of 160° relative to the beam's propagation direction. Two structural models of the layer stack were used to simulate the experimental spectra. One is a trilayer structure with abrupt interfaces (trilayer model). The second model consisted of 10 layers intended to account for the atomic diffusion and formation of intermediate buffer layers (gradient model). Figure 5a represents experimental and simulated spectra. It can be seen that each model describes the spectra (Figure 5a residual) well. However, the gradient model

results in a minor discrepancy to the experimental data in the channel regions of 275–310, which corresponds to the bottom of the lower $Fe_{3+x}Si_{1-x}$ and Ge layers. This fact allows us to conclude (Figure 5c) on the presence of a Ge-enriched layer between the Ge and $Fe_{3+x}Si_{1-x}$ layers and diffusion of the Fe into the Si substrate. The Ge content may reach ~38 at.% in the 2 nm interface region of the Ge layer with lower $Fe_{3+x}Si_{1-x}$. Germanium is incorporated into the upper layer of $Fe_{3+x}Si_{1-x}$ in less concentration, up to 18 at.% in 2 nm adjacent to the Ge intermediate layer (Figure 5c). Comparing interatomic distance misfits for the [−110] direction (Figure 5b) calculated based on the chemical composition distribution, one can see that the average misfit between both models differs by one per cent, which indicates that a more extended exposition to the elevated temperature of the $Fe_{3+x}Si_{1-x}$/Ge/$Fe_{3+x}Si_{1-x}$/Si(111) heterostructure may relieve the epitaxial stress. However, there must be a balance in the temperature-deposition rate and deposition time to obtain an all-epitaxial layer heterostructure with desired thicknesses. It may be seen that incorporation of Ge atoms in the lower $Fe_{3+x}Si_{1-x}$ silicide layer along with the Si atom diffusion from the substrate may relax the epitaxial stress of this layer with the silicon substrate, but conversely results in its increase with the upper germanium layer (Figure 5b). In turn, the germanium layer tends to reduce the interface area with the lower Ge-enriched $Fe_{3+x}Si_{1-x}$ silicide through the formation of 3D islands (Figure 1f).

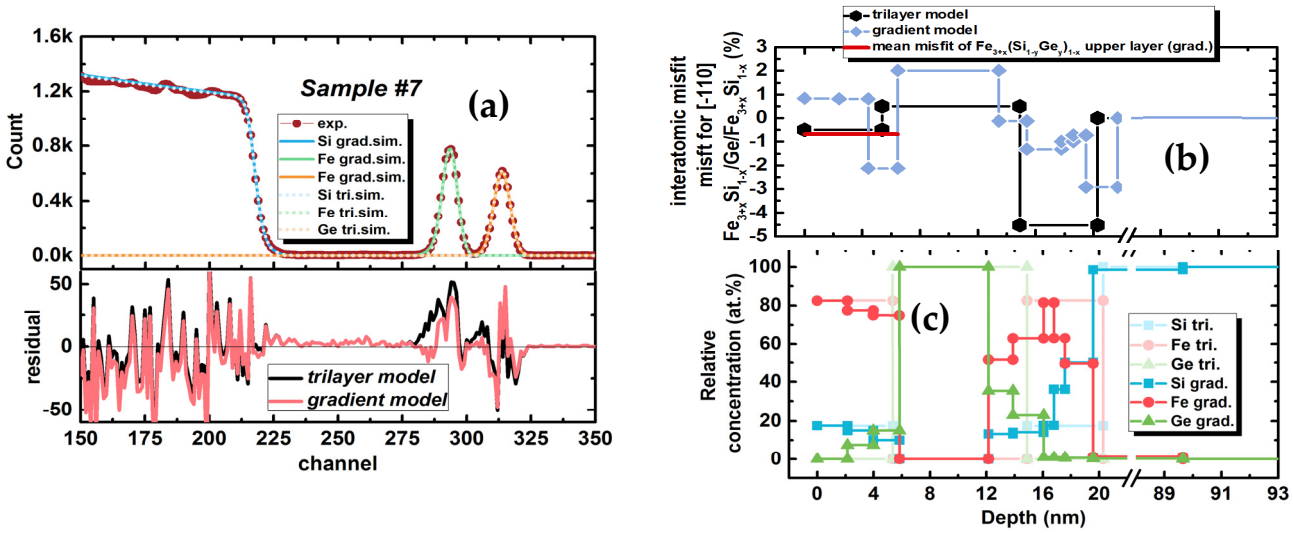

Figure 5. RBS spectra for $Fe_{3+x}Si_{1-x}$/Ge/$Fe_{3+x}Si_{1-x}$/Si(111) (sample #7) (**a**), misfits of each layer calculated based on the different fitting model of RBS spectra (**b**), a profile of relative chemical element concentration (at.%) derived from the RBS measurements for gradient and trilayer model (**c**).

It is worth noting that the observed asymmetry of peaks on spectrum corresponding to iron and germanium are not accounted for by the layer thickness variation of the trilayer model (Figure 6). The asymmetry of the peaks was assessed with the bigaussian function. The experimental values of widths of biguassian function defined in units of RBS channel are $w_{1(Fe)}$ = 3.3, $w_{2(Fe)}$ = 2.8, and $w_{1(Ge)}$ = 3.35, $w_{2(Ge)}$ = 3.08. While the trilayer model shows the closest value $w_{1(Fe)}$ = 2.83, $w_{2(Fe)}$ = 3.09, and $w_{1(Ge)}$ = 3.23, $w_{2(Ge)}$ = 3.09. The gradient model is better suited to describe the experimental data fitted with bigaussian function widths $w_{1,2(Fe,\,Ge)}$ equal to 3.28, 2.79, 3.28, and 2.8, respectively (Figure 6). Since the porosity of sample #7 reaches 17.3% (details are given below), the porosity was included in the simulation as a variable in the upper layers in the gradient and trilayer models. Simulations with porosity are excluded from the discussion since it does not change the simulated spectra noticeably.

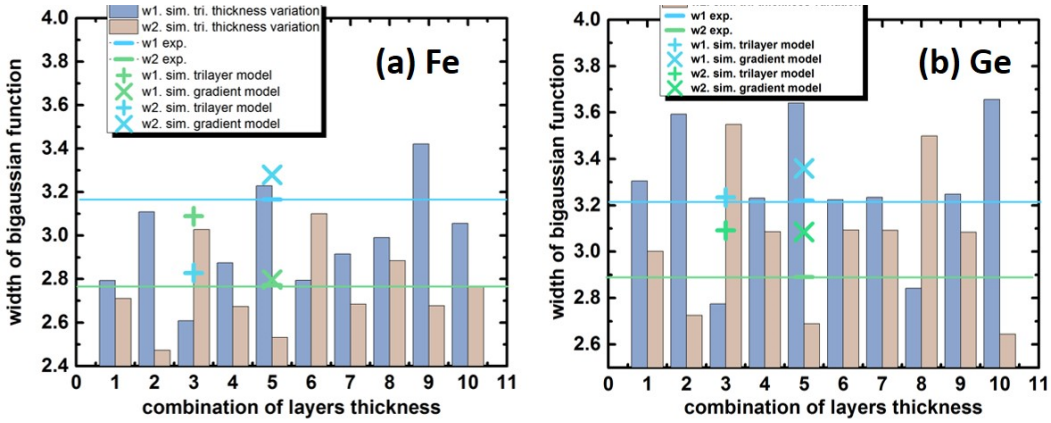

Figure 6. Analysis of asymmetry of the peaks of the RBS spectra for $Fe_{3+x}Si_{1-x}$/Ge/$Fe_{3+x}Si_{1-x}$/Si(111) (sample #7) with bigaussian function; blue and green lines refer to the experimental values of peak asymmetry observed for (**a**) Fe and (**b**) Ge; green marks corresponded to trilayer or gradient model fits as discussed; and bars indicate the asymmetry values for the different combinations of thickness in the trilayer model.

3.1.4. Surface Morphology and Dislocation Characteristics

We also characterized the topography by non-destructive atomic force microscopy (AFM). The distribution of roughness data is given in Table 3. Sample 7 is expected to have higher roughness due to the thicker Ge layer, the upper layer's polycrystalline nature, and more significant misfits of Ge with the underlying $Fe_{3+x}Si_{1-x}$ layer [20,41]. The value of residual stress discussed above and the measured RMS values can be compared with the ones reported elsewhere [42]. Areas of size 20 × 20 μm^2 and 2 × 2 μm^2 were examined, statistical parameters for each sample were calculated in three different areas, and the mean value was calculated. Scanning areas with a size of 20 × 20 μm^2 showed that the surface of the films is smooth, homogeneous, and does not have pronounced features. Figure 7a shows a typical topography of sample #7. When scanning a 2 × 2 μm^2 area with a higher resolution (~7.8 nm per pixel), it is possible to distinguish nano-sized depressions ("pits") on the film surface. Their surface density is different for samples #6 and #7, that is 17.3% and 43.1%, respectively. A significant difference in the thin surface morphology indicates different formation mechanisms for the samples discussed. Variation of the thermal history of the samples results in different levels of incorporation of Ge atoms into $Fe_{3+x}Si_{1-x}$ layers and causes variation of residual stress. The observable surface morphological characteristics are to be further analysed.

Table 3. Surface statistics parameters (over the entire scanning area).

	Scanning Area (μm)	Mean Value (nm)	RMS Roughness, Sq (nm)	Average Roughness Sa (nm)	Median, nm	Maximum Height Sz (nm)
#6	2 × 2	6.90	1.42	1.01	7.34	11.196
#6	20 × 20	1.198	0.284	0.228	1.22	2.44
#7	2 × 2	7.05	2.20	1.87	7.69	12.69
#7	20 × 20	4.58	1.12	0.91	4.61	9.21

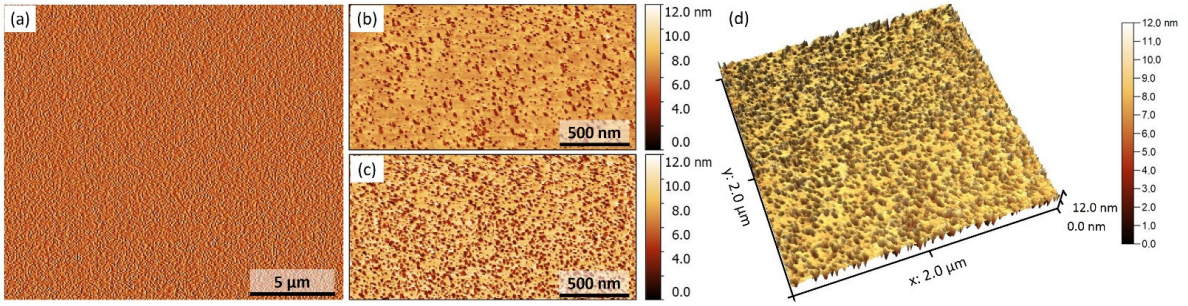

Figure 7. AFM images of the surface of $Fe_{3+x}Si_{1-x}$/Ge/$Fe_{3+x}Si_{1-x}$/Si(111) films. (**a**) A typical depiction of surface topology for sample #7; (**b**) for sample #6; (**c**) for sample #7; and (**d**) 3-d surface topology view for sample #6.

The typical pore size derived from the autocorrelated distribution function is 22.5 nm (Figure 8a), which is the same for both samples while the porosity of sample #7 is 2.5 times larger. Moreover, the pore size distribution is almost identical with the three most prominent pore sizes, which are 4.5, 18, and 25 nm (Figure 8c). Such a phenomenon refers to a different dominant mechanism of pore formation in epitaxial and polycrystalline upper $Fe_{3+x}Si_{1-x}$ layers. Under the condition of the same pore size, a sample with higher porosity would indicate less wettability of the surface, i.e., higher interface energy and lattice misfits. The forming layer tends to develop side facets and increase in bulk volume of 3D islands. The condition of the same amount of Fe–Si deposited should result in a different thickness of the upper $Fe_{3+x}Si_{1-x}$ layer. Otherwise, the Fe–Si are redistributed over the rough interface between the upper $Fe_{3+x}Si_{1-x}$ and intermediate Ge layers so that the thickness determined in a 2D projection measured with TEM remains the same in both samples (Figure 2).

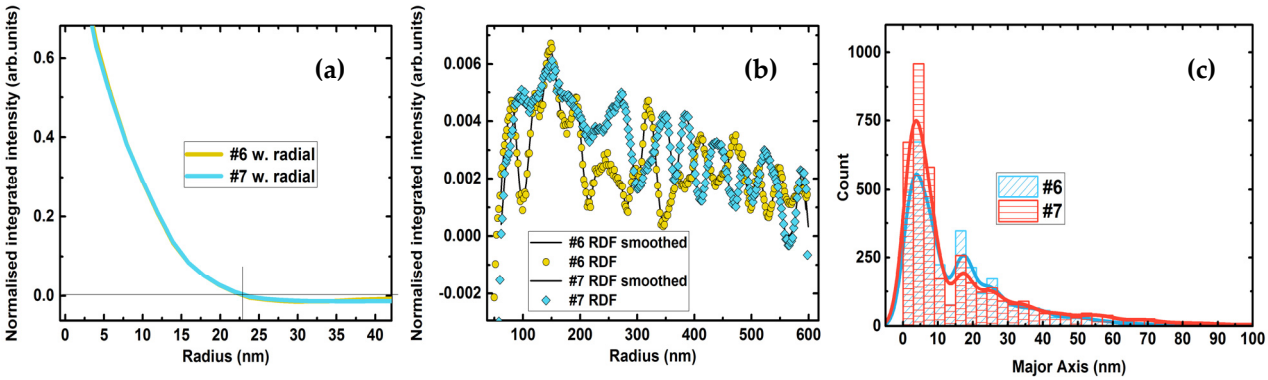

Figure 8. The radial average of the autocorrelation of pores from AFM images of the surface of $Fe_{3+x}Si_{1-x}$/Ge/$Fe_{3+x}Si_{1-x}$/Si(111) heterostructure. (**a**) The average pore size is close to 23 nm for both samples; (**b**) autocorrelated RDF for the samples #6 and #7 beyond the average pore size; and (**c**) distribution of pore size fitted with ellipses for the sample discussed.

Autocorrelated radial distribution function (RDF) for higher radii shows the prominent sharp peaks but with low probability (~0.01) (Figure 8b). It is also noticeable that the peaks in the 50–300 nm region between values are similar for both samples. The discrepancy in positions at higher radii may refer to the different spatial textures of overlapped pores. For the case of the epitaxial layer, the pore spatial distribution may correlate with the hexagonal lattice of the dislocation (Figure 9). The 2D dislocation lattice presented in Figure 9b was constructed by overlapping two lattices of stoichiometric Fe_3Si and silicon with the experimental OR [43]. Figure 9b also shows the distribution of near coincidence sites on the interface of stoichiometric iron silicide [33,44]. The structural motif of the spatial distribution of the dislocation borders can be easily observed on the dark field

images by the TEM technique in over-focus mode measured in plan view for the one 40 nm thick $Fe_{3+x}Si_{1-x}$ layer grown on Si(111) with the same procedure described above. The fast Fourier transform (Figure 9c) and distance between honeycomb borders (Figure 9d,f) observed correlate well with the expected interatomic misfit value of −4.8% along <110> (Figure 9e). Thus, the interface energy is supposed to increase at the awaited dislocation site, so a pore is predominantly located at such position until the amount of the deposited material allows growing a noncontinuous film under a given energy landscape. Since the epitaxial islands mostly form due to the Terrace–Ledge–Kink (TLK) mechanism [45] on the vicinal silicon surface (111), the density of the material can also be regulated by the average width of silicon terraces and show correlation with the average terrace width value. For the case of the polycrystalline film, the dislocation lattice should not affect the pore formation.

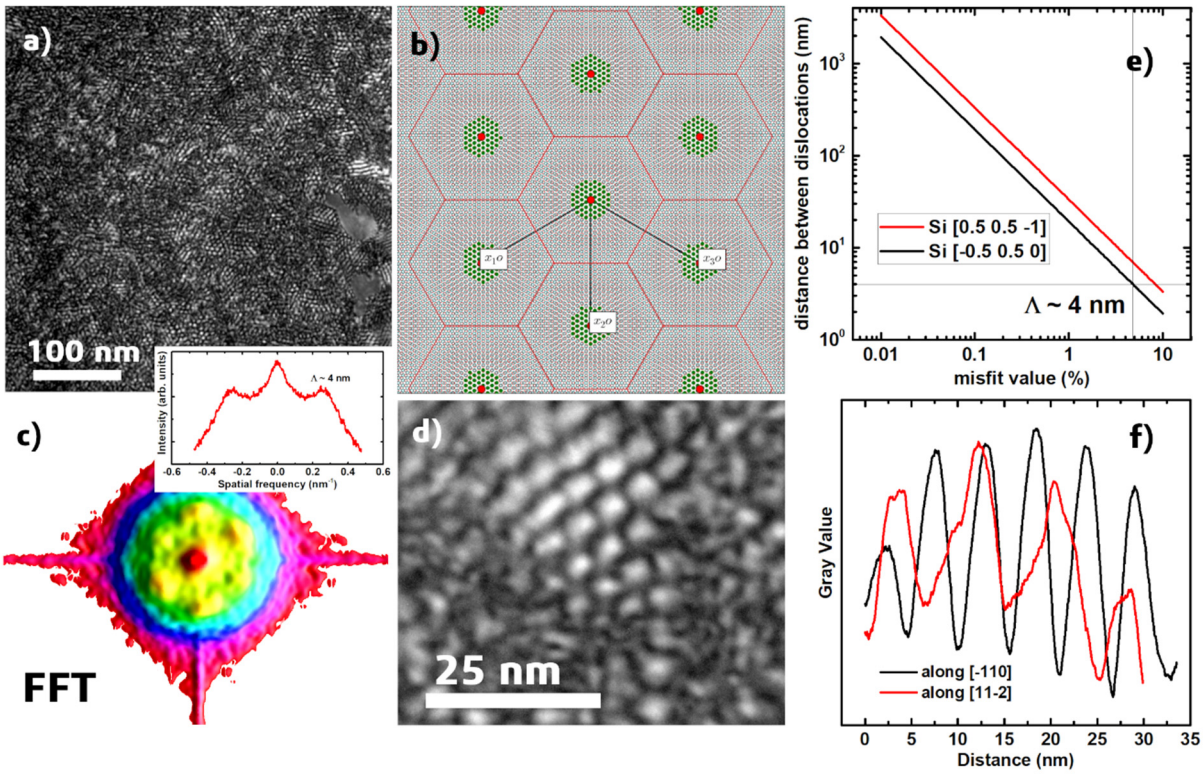

Figure 9. (**a**) A TEM plan-view image of one layer of $Fe_{3+x}Si_{1-x}$ grown on Si(111) (over-focus mode); (**b**) 2D O-lattice formed by overlapping two lattices, lattice points of which are represented by small, red circles (Si) and cyan circles (Fe_3Si), respectively. Each O-point (large circle) is at the centre of an O-cell (O-cell walls—solid lines), and near coincidence sites are depicted with green-filled circles; (**c**) FFT image in a 3D perspective view of Figure 9a. The inset depicts a line cut over the FFT image. (**d**) Magnified view of the structural motif of the dislocation lattice; (**e**) dependence of distance between dislocation along [−110] and [11−2] directions on misfit value for silicon; and (**f**) intensity distribution along two directions of the structural motif depicted on Figure 9d.

Here, we attempted to fit the autocorrelated RDF function with two simple models of hexagonal and rectangular lattice to indicate the mechanism of pore formation in the samples discussed. The hexagonal lattice corresponds to the dislocation sites for $Fe_{3+x}Si_{1-x}(111)||Ge(111)$ along <112> direction (Figure 9b). The square lattice corresponds to the terrace model. We used one hexagonal lattice and several rectangular lattices (1 × 1, 2 × 1, and 4 × 1). The RDF function is described with the sum of three Gaussian functions corresponding to the pore size distribution (Figure 8c). The fitted parameters are x, q, and w, where x refers to the scale, i.e., distances between pores, w is the parameter regulating the width of the Gaussian function, and q is the fraction of the hexagonal model. The *1-q* value is a fraction of the rectangular pore lattice. The uniformly distributed array of random values

of the fitted parameters with size 6×10^7 was used to find the standard deviation function. The figure presents the 2D kernel density of the STD value and functional parameter of x and q for both samples. The fitted w is close to the experimental values determined from the pore size distribution (Figure 8c).

Under the suggestion, the mechanism of distribution of the pores in all-epitaxial $Fe_{3+x}Si_{1-x}$/Ge/$Fe_{3+x}Si_{1-x}$/Si(111) trilayer (sample #6) discussed above are mainly governed by the hexagonal dislocation lattice (Figure 10), and in the polycrystalline layer of $Fe_{3+x}Si_{1-x}$ it should be affected by the TLK growth mode; then, one can determine the average dislocation distance along [11−2] or average terrace width of Si(111) surface. The fitting procedure of the autocorrelated RDF (Figure 8b) reveals that sample #6 is better described with the hexagonal lattice and vice versa sample #7 finds the best solution for almost pure terrace model (Figure 10) with average terrace width close to 17.7 nm. This value is in good agreement with the Si(111) miscut of the silicon wafer used in our experiments ($\pm 1^\circ$ as stated by the producer) [46,47].

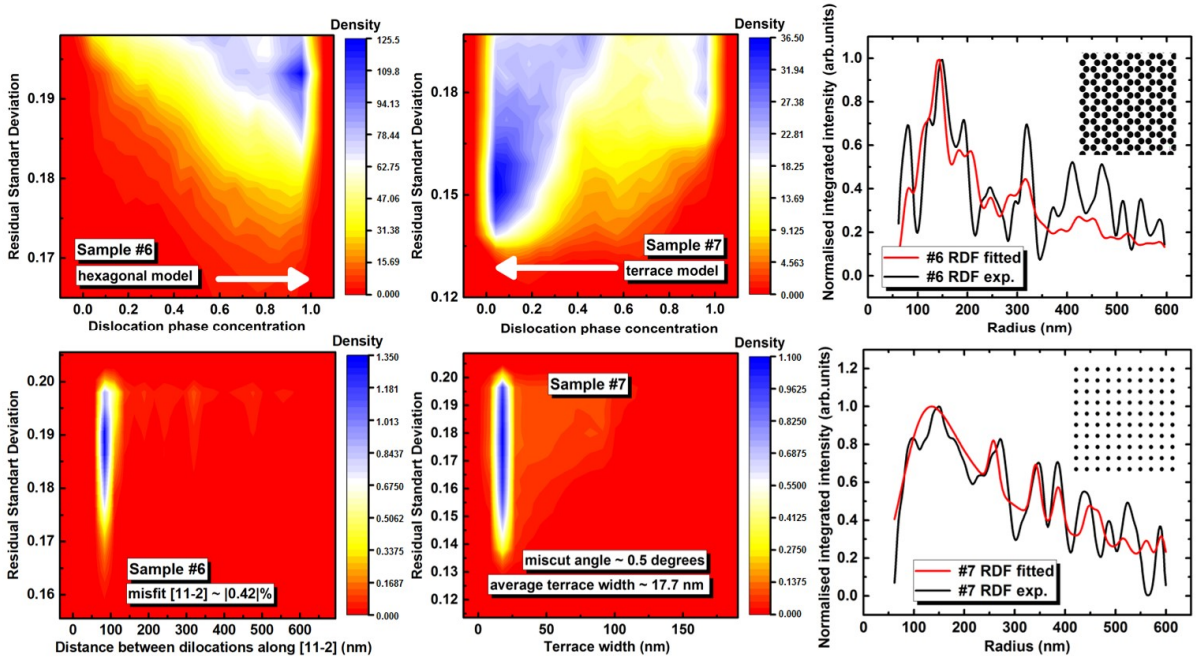

Figure 10. Dependence of 2D kernel density of residual standard deviation on random uniform distribution of sets fitting parameters of the autocorrelated RDF for both samples: (**upper left**) weight of pore distribution model (hexagonal or 1×1 square lattice or terrace), (**lower left**) distance between the dislocation along [11−2], sample #6; (**middle-upper**) weight of pore distribution model (hexagonal or terrace), (**middle-lower**) distance between average terrace width, sample #7; (**upper right**) the autocorrelated RDF fitted for the sample #7, (**right lower**), the autocorrelated RDF fitted for the sample #6; insets show the pore distribution model.

Thus, prolonged exposition of the $Fe_{3+x}Si_{1-x}$ bottom layer at the higher temperature of 300 °C causes increased atomic diffusion on the interfaces resulting in higher lattice misfits of Ge/$Fe_{3+x}Si_{1-x}$ due to the incorporation of Ge atoms into the $Fe_{3+x}Si_{1-x}$ bottom layer. The film develops a three-dimensional surface to lower the total free energy in heteroepitaxial thin film systems with biaxial stress. As a result, the growing Ge layer in the surface valley should show higher residual stress than at a peak, so incoming atoms preferably attach to the peak area, increasing the surface roughness. According to our estimation, the misfit value in the case of all-epitaxial trilayer structure (sample #6) is |0.42|%, which is close to the estimation of the misfit value based on the nominal composition of the layer with abrupt interfaces (Figure 5b). The misfit value for the germanium layer (sample #6) is expected to be also close to 0.42% while for the sample #7 with higher atomic diffusion, the

misfits for two upper layers are close −1% and 2% (Figure 5b). The iron-rich composition of the silicide without termination with ultra-thin silicon layer [11] also impacts increasing the interface energy. Altogether, this lowers the total energy through the developing surface and the transition to the polycrystalline growth while the growing layer remains textured with certain crystallites preserving higher residual stress than in the epitaxial layer. The texturing of the polycrystalline $Fe_{3+x}Si_{1-x}$ layer is expected to be due to the faceting of the monocrystalline Ge 3D islands.

3.2. Magnetic Properties

Differences in microstructure, degree of crystallinity, and residual stress should significantly affect magnetic properties [48,49], such as magnetization, coercive force, and anisotropy. Indeed, the saturation magnetization (Figure 11) of sample #6 with 4 nm thick Ge ("Ge 4 nm") is 40% higher than that of sample # 7. The coercive force H_C for this sample is almost three times lower (0.145 mT), while for sample #7 with 7 nm thick Ge ("Ge 7 nm"), it is 0.403 mT. In addition, sample #7 "Ge 7 nm" demonstrates some features of magnetization reversal indicated by arrows in Figure 11, which may be associated with the presence of additional ferromagnetic phases, disordered A2 Fe–Ge–Si alloys formed near the interfaces, non-stoichiometric composition, and imperfection of the crystal structure of the upper $Fe_{3+x}Si_{1-x}$ layer. Moreover, lower $Fe_{3+x}Si_{1-x}$ layers can also be different due to a two-times more extended exposition at elevated temperature of "Ge 7 nm" sample that leads more complex interface structure and composition on the lower $Ge/Fe_{3+x}Si_{1-x}$ and $Fe_{3+x}Si_{1-x}/Si$ boundaries resulting to decreasing of saturation magnetisation M_S other loop's features.

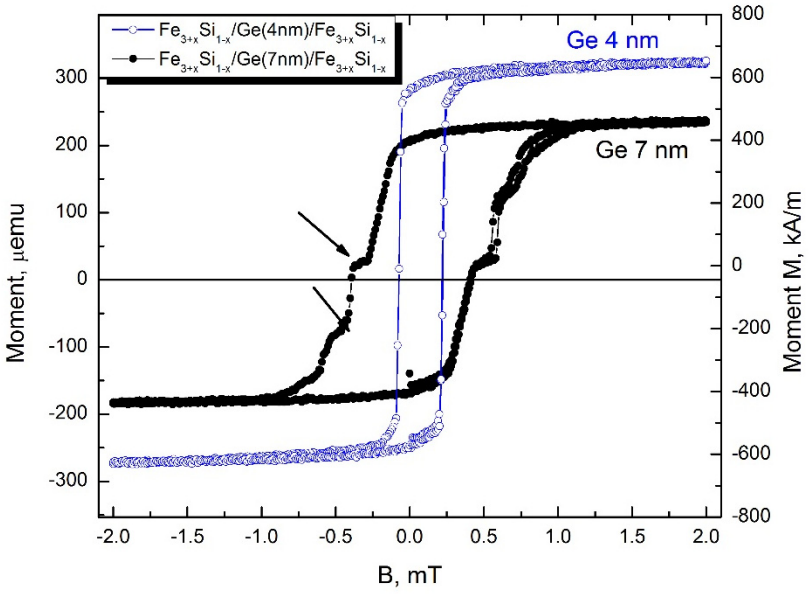

Figure 11. In-plane magnetization reversal of $Fe_{3+x}Si_{1-x}$/Ge(4 nm)/$Fe_{3+x}Si_{1-x}$ and $Fe_{3+x}Si_{1-x}$/Ge(8 nm)/$Fe_{3+x}Si_{1-x}$ structures at 300 K.

To determine the magnetic anisotropy, we measured the angular dependence of the ferromagnetic resonance (FMR) spectra both in the plane and perpendicular to the plane at a temperature of 300 K. The spectrum (Figure 12a) for sample #6 "Ge 4 nm" shows two absorption lines, which, given the RHEED and TEM data, most likely correspond to FMR of the upper and lower $Fe_{3+x}Si_{1-x}$ films. For sample #7 "Ge 7 nm" (Figure 12a), the second line is less pronounced and consists of two, potentially three, absorption lines. We analysed the angular dependence of all five lines (Figure 12b–f). The structure has an easy plane magnetization due to shape anisotropy. In addition, polar dependences reveal no magnetic coupling between upper and lower films of iron silicide. In particular,

crossing of lines was observed during sweeping of out-of-plane angle. It occurs due to films having different M_S and corresponding shape anisotropy filed $4\pi \cdot M_S$. Secondly, the angular in-plane dependence of the resonance field is characteristically different for all resonances (Figure 12).

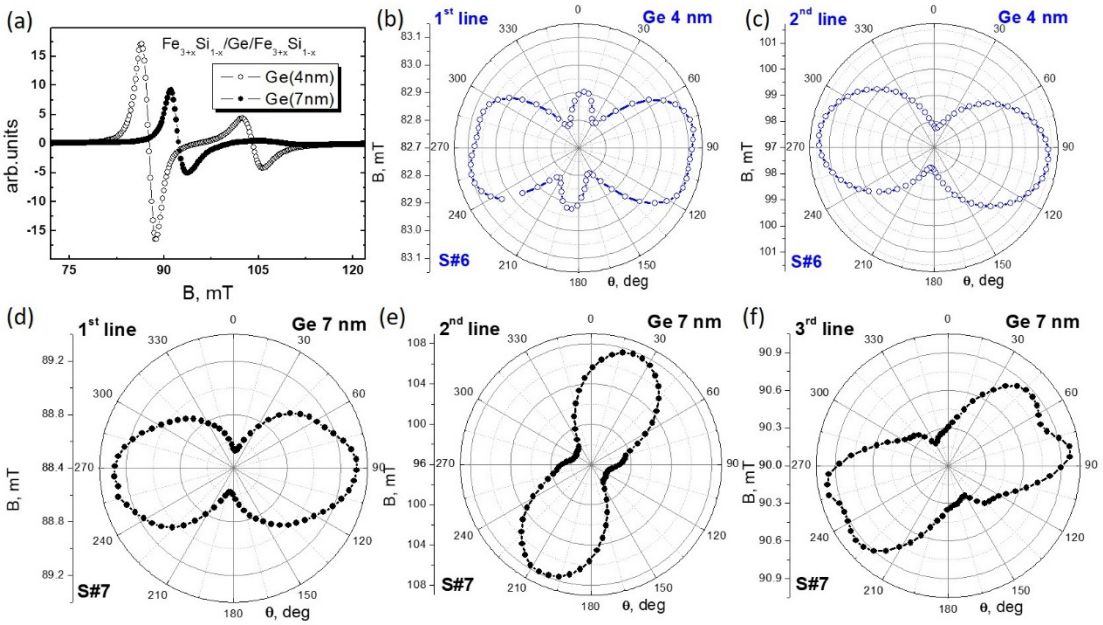

Figure 12. (**a**) FMR spectra of $Fe_{3+x}Si_{1-x}$/Ge(4 nm)/$Fe_{3+x}Si_{1-x}$ (**a**) and $Fe_{3+x}Si_{1-x}$/Ge(7 nm)/$Fe_{3+x}Si_{1-x}$ structures. Polar plots of angular dependences of 1st (**b**) and 2nd (**c**) lines of $Fe_{3+x}Si_{1-x}$/Ge(4 nm)/$Fe_{3+x}Si_{1-x}$ structure and 1st (**d**), 2nd (**e**), and 3rd (**f**) lines of $Fe_{3+x}Si_{1-x}$/Ge(7 nm)/$Fe_{3+x}Si_{1-x}$ structure.

Using the conventional analysis [50,51], we calculate the different contributions to the magnetic anisotropy (Table 4): saturation magnetization (M_S), anisotropy field (H_K), and anisotropy angle (α_K) measured relative to the direction of uniaxial anisotropy, that is, the easy magnetization axis of the 1st line for each of the samples. It is worth noting that the M_S value of the 1st line derived from the resonance field is comparable to high-quality epitaxial $Fe_{3+x}Si_{1-x}$ films grown separately on different substrates (see for example [35,40,52]). For the 2nd line, M_S is smaller due to the deterioration of the crystalline quality of the upper film. The nature of the third line in sample #7 "Ge 7 nm" is associated with the imperfection of the upper $Fe_{3+x}Si_{1-x}$ layer and the presence of Fe–Si–Ge alloy at the interfaces. The uniaxial in-plane anisotropy is the dominating contribution. This behaviour was observed earlier for (111) $Fe_{3+x}Si_{1-x}$ films [53] and can be related to the surface of the Si substrate and Si(111)/Fe_{3+x}/Si_{1-x}(111) interface effects. Another reason may be associated with the features of an oblique deposition, which were observed earlier in Fe and other iron silicide films [54]. Nonetheless, we observe uniaxial anisotropy for sample #7 "Ge 7 nm". If oblique deposition is the reason for the uniaxial anisotropy, it should be the same for all grown films. From the variation of the symmetry axis between films we conclude that the anisotropy directions are due to crystalline features in the layers not produced by oblique incidence of the atoms during growth.

Table 4. Parameters of FMR lines and contributions of anisotropy of three-layer structures.

Ge			Anisotropy					
		Magnetization Saturation	Uniaxial		Four-Fold		Six-Fold	
	Sample	Ms, kA/m	Hk2, mT	αk2, deg.	Hk4, mT	Tk4, deg.	Hk6, mT	αk6, deg.
4 nm	1st line	1034.04	0.153	**0**	0.043	−41.29	0.058	−85.55
	2nd line	835.99	1.925	7.13	0.117	−81.27	0.058	−115.09
7 nm	1st line	955.13	0.366	**0**	0.046	−73.49	0.033	−52.04
	2nd line	814.07	5.613	−65.13	1.085	−25.42	0.210	−97.22
	3rd line	935.24	0.378	−23.39	0.0078	−76.28	0.043	−59.06

There is also a noticeable 6th order contribution Hk_6 (Table 4) along with the cubic Hk_4 (4th order) symmetry axis [52,55,56]. For example, for lines presented on Figure 12b we found that Hk_6 is greater than Hk_4. Moreover, Hk_6 is only 2.7 times lower than uniaxial Hk_2 contribution. The reason for this is that both the upper and lower $Fe_{3+x}Si_{1-x}$ films have an epitaxial relation with the Si (111) | | $Fe_{3+x}Si_{1-x}$ (111), which means that we observe the anisotropy of the (111) $Fe_{3+x}Si_{1-x}$ crystal, which has a six-fold crystal symmetry (Figure 2c).

3.3. Transport Properties

In addition to certain magnetic properties, three-layer FM/SC/FM structures must also have specific transport properties. In particular, the SC layer must exhibit semiconducting transport properties, which is important for controlling spin transport using an electric field or, for example, optical irradiation. Using etching in an HF: HNO_3: H_2O = 1: 2: 400 solution, we prepared samples with contacts made from the $Fe_{3+x}Si_{1-x}$ film on the Ge surface (inset in Figure 13) to measure the temperature dependences of the Ge resistance and compare it with the films of different thicknesses. The distance between $Fe_{3+x}Si_{1-x}$ contacts was 500 μm. Note that the contact remains ohmic up to 5 K, i.e., the *I*–*V* curves are linear over the entire temperature range for both samples. The resistance R of sample #6 "Ge 4 nm" increases nonlinearly with decreasing temperature rising by about a factor of 3 at 5 K compared with R at 300 K (left panel in Figure 13). At the same time, sample #7 "Ge 7 nm" demonstrates a completely different behaviour; upon cooling, its resistance first decreases monotonically, reaching a minimum at 55 K, and then increases (right panel in Figure 13). Moreover, the relative changes are minimal. The ratio of the minimum resistance to the room temperature resistance R_{min}/R_{300} is 0.95, which is a 5% change. Over the entire temperature range, resistance changes for only 2.5% (R_5/R_{300} = 0.975).

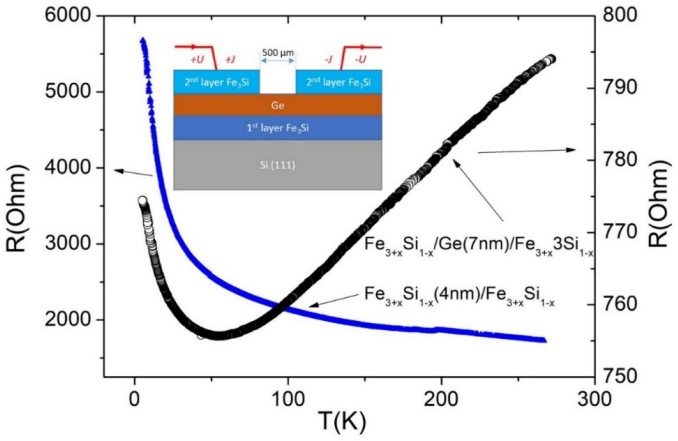

Figure 13. Temperature dependences of resistance of $Fe_{3+x}Si_{1-x}$/Ge(4 nm)/$Fe_{3+x}Si_{1-x}$ and $Fe_{3+x}Si_{1-x}$/Ge(7 nm)/$Fe_{3+x}Si_{1-x}$ etched structures.

It can be seen from Figure 13 that the temperature dependence of the resistance for sample #6 "Ge 4 nm" is due to the conductivity of the thermoactivation type. However, fitting in Arrhenius coordinates (ln (R) vs. 1/T) does not give a good linear fit. The best linearization is obtained using $R = R_0 \exp(T_0/T^{1/4})$ (Figure 14), which suggests that the hopping type of conduction with variable hopping length (VRH) [57] prevails over the thermal delocalization of carriers and their transfer to the conduction band of germanium. The calculated parameter T_0 is 65 K, which is typical for "inhomogeneous" materials [58]. The dominance of the VRH mechanism is most likely due to the small thickness of the Ge interlayer and, accordingly, the high density of defects, that may indicate a partial island-like character of the film. Measured magnetoresistance curves R(H) at temperature 4 K in parallel and perpendicular magnetic field (not shown here) found no differences that is an additional argument for the 3-dimensional VRH transport mechanism.

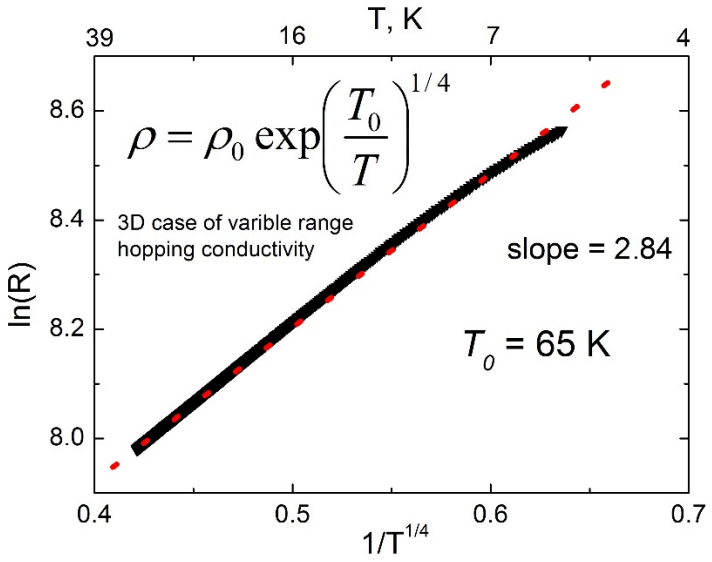

Figure 14. Fitting of temperature dependence of resistance of $Fe_{3+x}Si_{1-x}$/Ge(4 nm)/$Fe_{3+x}Si_{1-x}$ etched structure.

The resistance of sample #7 "Ge 7 nm" resembles a degenerate semiconductor. Considering slight changes with temperature (R_5/R_{300} = 0.975), we believe that a decrease in resistance in the temperature range from 300 K to 55 K is associated with an increase in the mobility of charge carriers due to a decrease in electron-phonon scattering. When analysing the low-temperature part of the curve, we tried various models such as the thermally activated behaviour (ln(R)~1/T), thermoactivated tunnelling between nearest grains in a granular system (ln(R)~$1/T^{1/2}$) [59], and the VRH (ln(R)~$1/T^{1/4}$) behaviour for fitting. However, none of these models fit the experimental data well. It can be assumed that an increase in resistance below 55 K might be caused by scattering of magnetic impurities, i.e., Kondo scattering [60]. As it was shown, Fe impurities are likely to be present at the Ge/$Fe_{3+x}Si_{1-x}$ interfaces. Another reason may be the manifestation of quantum corrections to the conductivity at low temperatures [61].

4. Conclusions

Epitaxial $Fe_{3+x}Si_{1-x}$/Ge/$Fe_{3+x}Si_{1-x}$ trilayers with 4 and 7 nm Ge layer thickness were grown. At a higher temperature of 300 °C during the formation of the Ge layer, we found a larger lattice misfit at the Ge/$Fe_{3+x}Si_{1-x}$ interface and the development of a rough interface due to the incorporation of Ge atoms into the $Fe_{3+x}Si_{1-x}$ bottom layer. We demonstrate the epitaxial growth of an iron-rich $Fe_{3+x}Si_{1-x}$ upper layer on the germanium layer with thickness of 4 nm. With increasing Ge thickness, the upper $Fe_{3+x}Si_{1-x}$ layer becomes polycrystalline and with a rougher surface.

The ferromagnetic resonance study revealed magnetic crystal anisotropy with a six-fold symmetry typical for the (111) plane of $Fe_{3+x}Si_{1-x}$. This fact indicates the probable epitaxial ratio $Fe_{3+x}Si_{1-x}(111)[0-11]$ || $Ge(111)[1-10]$ || $Fe_{3+x}Si_{1-x}(111)[0-11]$ || $Si(111)[1-10]$. The resistance of the Ge layer measured on specially prepared structures demonstrates an increase with decreasing temperature, reflecting its semiconductor nature. With an increase in the Ge thickness to 7 nm, the transport properties become similar to a degenerate semiconductor due to intermixing iron, germanium, and silicon atoms in disordered interfaces.

Our work showed that in the iron-rich $Fe_{3+x}Si_{1-x}/Ge/Fe_{3+x}Si_{1-x}$ system, a high crystalline perfection of individual layers can be obtained while maintaining the semiconducting properties of the Ge layer. At the same time, an increase in the semiconductor layer thickness from 4 nm to 7 nm leads to a significant change in the magnetic properties of the upper ferromagnetic layer, yielding the opportunity to vary its magnetization by controlling the Ge thickness. Additionally, we discussed the limits of the all-epitaxial formation of the iron-rich $Fe_{3+x}Si_{1-x}/Ge/Fe_{3+x}Si_{1-x}$ heterostructures and its relation to the structural, magnetic, and transport properties.

Author Contributions: Conceptualization, A.S.T., I.A.T. and N.V.V.; methodology, I.A.T. and S.N.V.; software, I.A.T.; validation, M.V.R.; formal analysis, B.A.B. and F.A.B.; investigation, I.A.Y., M.V.R., I.A.B., A.V.L., M.S.P., L.V.S., D.D.E. and M.N.V.; resources, A.Y.G. and S.G.O.; data curation, A.S.T., M.V.R. and I.A.T.; writing—original draft preparation, A.S.T., I.A.T. and A.V.L.; writing—review and editing, M.V.R., I.A.T. and M.F.; visualization, I.A.B.; supervision, A.S.T. and I.A.T.; project administration, S.N.V. and A.S.T.; and funding acquisition, S.G.O. and M.F. All authors have read and agreed to the published version of the manuscript.

Funding: The research was funded by RFBR, Krasnoyarsk Territory, and Krasnoyarsk Regional Fund of Science, project number 20-42-243007, and by the Government of the Russian Federation, Mega Grant for the Creation of Competitive World-Class Laboratories (Agreement no. 075-15-2019-1886). I.A.T. and S.N.V. thank RFBR, Krasnoyarsk Territory, and Krasnoyarsk Regional Fund of Science, project number 20-42-240012, for partial work related to the development of the simulation model of the pore autocorrelated radial distribution function coupled with the near coincidence site model, the $Fe_{3+x}Si_{1-x}$ lattice distortion analysis, and processing Rutherford backscattering spectroscopy data. The Rutherford backscattering spectroscopy measurements were supported by the Ministry of Science and Higher Education of the Russian Federation (project FZWN-2020-0008).

Institutional Review Board Statement: Not applicable.

Informed Consent Statement: Not applicable.

Data Availability Statement: Not applicable.

Conflicts of Interest: The authors declare no conflict of interest.

References

1. Bhatti, S.; Sbiaa, R.; Hirohata, A.; Ohno, H.; Fukami, S.; Piramanayagam, S.N. Spintronics based random access memory: A review. *Mater. Today* **2017**, *20*, 530–548. [CrossRef]
2. Jansen, R. Silicon spintronics. *Nat. Mater.* **2012**, *11*, 400–408. [CrossRef]
3. Liu, W.; Wong, P.K.J.; Xu, Y. Hybrid spintronic materials: Growth, structure and properties. *Prog. Mater. Sci.* **2019**, *99*, 27–105. [CrossRef]
4. Tanaka, M.; Sugahara, S. MOS-Based Spin Devices for Reconfigurable Logic. *IEEE Trans. Electron Devices* **2007**, *54*, 961–976. [CrossRef]
5. Nikonov, D.E.; Young, I.A. Overview of Beyond-CMOS Devices and a Uniform Methodology for Their Benchmarking. *Proc. IEEE* **2013**, *101*, 2498–2533. [CrossRef]
6. Wollmann, L.; Nayak, A.K.; Parkin, S.S.P.; Felser, C. Heusler 4.0: Tunable Materials. *Annu. Rev. Mater. Res.* **2017**, *47*, 247–270. [CrossRef]
7. Draganyuk, O.N.; Zhandun, V.S.; Zamkova, N.G. Half-metallicity in Fe_2MnSi and Mn_2FeSi heusler compounds: A comparative ab initio study. *Mater. Chem. Phys.* **2021**, *271*, 124897. [CrossRef]
8. Kumar, A.; Pan, F.; Husain, S.; Akansel, S.; Brucas, R.; Bergqvist, L.; Chaudhary, S.; Svedlindh, P. Temperature-dependent Gilbert damping of Co_2FeAl thin films with different degree of atomic order. *Phys. Rev. B* **2017**, *96*, 224425. [CrossRef]

9. Srinivas, K.; Raja, M.M.; Rao, D.S.; Kamat, S.V. Effect of sputtering pressure and power on composition, surface roughness, microstructure and magnetic properties of as-deposited Co_2FeSi thin films. *Thin Solid Film.* **2014**, *558*, 349–355. [CrossRef]
10. Liu, Y.C.; Chen, Y.W.; Tseng, S.C.; Chang, M.T.; Lo, S.C.; Lin, Y.H.; Cheng, C.K.; Hung, H.Y.; Hsu, C.H.; Kwo, J.; et al. Epitaxial ferromagnetic Fe_3Si on GaAs(111)A with atomically smooth surface and interface. *Appl. Phys. Lett.* **2015**, *107*, 122402. [CrossRef]
11. Sakai, S.; Kawano, M.; Ikawa, M.; Sato, H.; Yamada, S.; Hamaya, K. Low-temperature growth of fully epitaxial CoFe/Ge/Fe_3Si layers on Si for vertical-type semiconductor spintronic devices. *Semicond. Sci. Technol.* **2017**, *32*, 094005. [CrossRef]
12. Shiihara, T.; Oki, S.; Sakai, S.; Ikawa, M.; Yamada, S.; Hamaya, K. Epitaxial growth of Sb-doped Ge layers on ferromagnetic Fe_3Si for vertical semiconductor spintronic devices. *Semicond. Sci. Technol.* **2018**, *33*, 104008. [CrossRef]
13. Gaucher, S.; Jenichen, B.; Kalt, J.; Jahn, U.; Trampert, A.; Herfort, J. Growth of Fe_3Si/Ge/Fe_3Si trilayers on GaAs(001) using solid-phase epitaxy. *Appl. Phys. Lett.* **2017**, *110*, 102103. [CrossRef]
14. Toriumi, A.; Nishimura, T. Germanium CMOS potential from material and process perspectives: Be more positive about germanium. *Jpn. J. Appl. Phys.* **2018**, *57*, 010101. [CrossRef]
15. Hamaya, K.; Fujita, Y.; Yamada, M.; Kawano, M.; Yamada, S.; Sawano, K. Spin transport and relaxation in germanium. *J. Phys. D Appl. Phys.* **2018**, *51*, 393001. [CrossRef]
16. Froning, F.N.M.; Camenzind, L.C.; van der Molen, O.A.H.; Li, A.; Bakkers, E.P.A.M.; Zumbühl, D.M.; Braakman, F.R. Ultrafast hole spin qubit with gate-tunable spin–orbit switch functionality. *Nat. Nanotechnol.* **2021**, *16*, 308–312. [CrossRef]
17. Wang, Z.; Marcellina, E.; Hamilton, A.R.; Cullen, J.H.; Rogge, S.; Salfi, J.; Culcer, D. Optimal operation points for ultrafast, highly coherent Ge hole spin-orbit qubits. *npj Quantum Inf.* **2021**, *7*, 54. [CrossRef]
18. Yamada, S.; Tanikawa, K.; Miyao, M.; Hamaya, K. Atomically Controlled Epitaxial Growth of Single-Crystalline Germanium Films on a Metallic Silicide. *Cryst. Growth Des.* **2012**, *12*, 4703–4707. [CrossRef]
19. Jenichen, B.; Herfort, J.; Jahn, U.; Trampert, A.; Riechert, H. Epitaxial Fe_3Si/Ge/Fe_3Si thin film multilayers grown on GaAs(001). *Thin Solid Film.* **2014**, *556*, 120–124. [CrossRef]
20. Kawano, M.; Yamada, S.; Tanikawa, K.; Sawano, K.; Miyao, M.; Hamaya, K. An ultra-thin buffer layer for Ge epitaxial layers on Si. *Appl. Phys. Lett.* **2013**, *102*, 121908. [CrossRef]
21. Karel, J.; Juraszek, J.; Minar, J.; Bordel, C.; Stone, K.H.; Zhang, Y.N.; Hu, J.; Wu, R.Q.; Ebert, H.; Kortright, J.B.; et al. Effect of chemical order on the magnetic and electronic properties of epitaxial off-stoichiometry Fe_xSi_{1-x} thin films. *Phys. Rev. B* **2015**, *91*, 144402. [CrossRef]
22. Karel, J.; Bouma, D.S.; Martinez, J.; Zhang, Y.N.; Gifford, J.A.; Zhang, J.; Zhao, G.J.; Kim, D.R.; Li, B.C.; Huang, Z.Y.; et al. Enhanced spin polarization of amorphous $FexSi_{1-x}$ thin films revealed by Andreev reflection spectroscopy. *Phys. Rev. Mater.* **2018**, *2*, 064411. [CrossRef]
23. Mehl, M.J. A Brief History of Strukturbericht Symbols and Other Crystallographic Classification Schemes. *J. Phys. Conf. Ser.* **2019**, *1290*, 012016. [CrossRef]
24. Schindelin, J.; Arganda-Carreras, I.; Frise, E.; Kaynig, V.; Longair, M.; Pietzsch, T.; Preibisch, S.; Rueden, C.; Saalfeld, S.; Schmid, B.; et al. Fiji: An open-source platform for biological-image analysis. *Nat. Methods* **2012**, *9*, 676–682. [CrossRef]
25. Volkov, N.V.; Tarasov, A.S.; Rautskii, M.V.; Lukyanenko, A.V.; Bondarev, I.A.; Varnakov, S.N.; Ovchinnikov, S.G. Magneto-transport phenomena in metal/SiO_2/n(p)-Si hybrid structures. *J. Magn. Magn. Mater.* **2018**, *451*, 143–158. [CrossRef]
26. Fultz, B.; Howe, J. Diffraction Contrast in TEM Images. In *Transmission Electron Microscopy and Diffractometry of Materials*; Springer: Berlin/Heidelberg, Germany, 2012; pp. 337–421.
27. Layadi, A. Effect of multiaxial stress in thin films on the ferromagnetic resonance mode characteristics. *J. Appl. Phys.* **2020**, *127*, 223907. [CrossRef]
28. Gueye, M.; Zighem, F.; Belmeguenai, M.; Gabor, M.; Tiusan, C.; Faurie, D. Ferromagnetic resonance in thin films submitted to multiaxial stress state: Application of the uniaxial equivalent stress concept and experimental validation. *J. Phys. D Appl. Phys.* **2016**, *49*, 265001. [CrossRef]
29. Dahlqvist, M.; Rosen, J. Impact of strain, pressure, and electron correlation on magnetism and crystal structure of Mn2GaC from first-principles. *Sci. Rep.* **2020**, *10*, 11384. [CrossRef] [PubMed]
30. Edington, J.W. Electron Diffraction in the Electron Microscope. In *Electron Diffraction in the Electron Microscope*; Macmillan Education: London, UK, 1975; pp. 1–77.
31. Klinger, M. More features, more tools, more CrysTBox. *J. Appl. Crystallogr.* **2017**, *50*, 1226–1234. [CrossRef]
32. Frentrup, M.; Hatui, N.; Wernicke, T.; Stellmach, J.; Bhattacharya, A.; Kneissl, M. Determination of lattice parameters, strain state and composition in semipolar III-nitrides using high resolution X-ray diffraction. *J. Appl. Phys.* **2013**, *114*, 213509. [CrossRef]
33. Visotin, M.A.; Tarasov, I.A.; Fedorov, A.S.; Varnakov, S.N.; Ovchinnikov, S.G. Prediction of orientation relationships and interface structures between α-, β-, γ-$FeSi_2$ and Si phases. *Acta Crystallogr. Sect. B Struct. Sci. Cryst. Eng. Mater.* **2020**, *76*, 469–482. [CrossRef]
34. Sandalov, I.; Zamkova, N.; Zhandun, V.; Tarasov, I.; Varnakov, S.; Yakovlev, I.; Solovyov, L.; Ovchinnikov, S. Effect of electron correlations on the Fe_3Si and $\alpha-FeSi_2$ band structure and optical properties. *Phys. Rev. B* **2015**, *92*, 205129. [CrossRef]
35. Tarasov, A.S.; Lukyanenko, A.V.; Tarasov, I.A.; Bondarev, I.A.; Smolyarova, T.E.; Kosyrev, N.N.; Komarov, V.A.; Yakovlev, I.A.; Volochaev, M.N.; Solovyov, L.A.; et al. Approach to form planar structures based on epitaxial $Fe_{1-x}Si_x$ films grown on Si(111). *Thin Solid Film.* **2017**, *642*, 20–24. [CrossRef]
36. Ingber, L. Adaptive simulated annealing (ASA): Lessons learned. *Control Cybern.* **2000**, *25*, 32–54.

37. Lagarias, J.C.; Reeds, J.A.; Wright, M.H.; Wright, P.E. Convergence Properties of the Nelder–Mead Simplex Method in Low Dimensions. *SIAM J. Optim.* **1998**, *9*, 112–147. [CrossRef]
38. Giannozzi, P.; Baroni, S.; Bonini, N.; Calandra, M.; Car, R.; Cavazzoni, C.; Ceresoli, D.; Chiarotti, G.L.; Cococcioni, M.; Dabo, I.; et al. Quantum Espresso: A Modular and Open-Source Software Project for Quantum Simulations of Materials. *J. Phys. Condens. Matter* **2009**, *21*, 395502. [CrossRef]
39. Perdew, J.P.; Burke, K.; Ernzerhof, M. Generalized Gradient Approximation Made Simple. *Phys. Rev. Lett.* **1996**, *77*, 3865–3868. [CrossRef]
40. Tarasov, A.S.; Lukyanenko, A.V.; Rautskii, M.V.; Bondarev, I.A.; Smolyakov, D.A.; Tarasov, I.A.; Yakovlev, I.A.; Varnakov, S.N.; Ovchinnikov, S.G.; Baron, F.A.; et al. Spin-dependent electrical hole extraction from low doped p-Si via the interface states in a Fe_3Si/p-Si structure. *Semicond. Sci. Technol.* **2019**, *34*, 035024. [CrossRef]
41. Wang, Y.; Li, J.; Li, S.; Chen, H.; Liu, D.; Kang, J. X-ray reflectivity and atomic force microscopy studies of MOCVD grown $Al_xGa_{1-x}N$/GaN superlattice structures. *J. Semicond.* **2011**, *32*, 043006. [CrossRef]
42. Kim, Y.; Yoon, S.; Ko, D.; Sohn, H. Influence of Si precursor type on the surface roughening of SiGe epitaxial layers deposited by ultrahigh vacuum chemical vapor deposition method. *J. Vac. Sci. Technol. A Vac. Surf. Film.* **2017**, *35*, 041403. [CrossRef]
43. Gu, X.F.; Furuhara, T.; Zhang, W.Z. PTCLab: Free and open-source software for calculating phase transformation crystallography. *J. Appl. Crystallogr.* **2016**, *49*, 1099–1106. [CrossRef]
44. Tarasov, I.A.; Smolyarova, T.E.; Nemtsev, I.V.; Yakovlev, I.A.; Volochaev, M.N.; Solovyov, L.A.; Varnakov, S.N.; Ovchinnikov, S.G. Tailoring the preferable orientation relationship and shape of α-$FeSi_2$nanocrystals on Si(001): The impact of gold and the Si/Fe flux ratio, and the origin of α/Si boundaries. *CrystEngComm* **2020**, *22*, 3943–3955. [CrossRef]
45. Bhukta, A.; Levi, G.; Horvitz, D.; Kohn, A.; Goldfarb, I. Self-organized exchange-spring magnet in epitaxial β-Fe(Ni)Si_2/Si system. *Appl. Surf. Sci.* **2021**, *562*, 150071. [CrossRef]
46. Bellucci, S. *Self-Assembly of Nanostructures: The INFN Lectures*; Springer: Berlin/Heidelberg, Germany, 2011; Volume 3, ISBN 9781461407423.
47. Wang, X.S.; Goldberg, J.L.; Bartelt, N.C.; Einstein, T.L.; Williams, E.D. Terrace-width distributions on vicinal Si(111). *Phys. Rev. Lett.* **1990**, *65*, 2430–2433. [CrossRef] [PubMed]
48. Xie, J.; Liao, Y.-F.; Wu, D.-N.; Xiao, W.-J.; Xie, Q. The Degree-of-Order Dependent Electronic Structures and Magnetic Properties of Fe_3Si Alloys. *Phys. Status Solidi* **2020**, *257*, 1900667. [CrossRef]
49. Zamkova, N.G.; Zhandun, V.S.; Ovchinnikov, S.G.; Sandalov, I.S. Effect of local environment on moment formation in iron silicides. *J. Alloys Compd.* **2017**, *695*, 1213–1222. [CrossRef]
50. Belyaev, B.A.; Izotov, A.V.; Leksikov, A.A. Magnetic imaging in thin magnetic films by local spectrometer of ferromagnetic resonance. *IEEE Sens. J.* **2005**, *5*, 260–267. [CrossRef]
51. Yakovlev, I.A.; Tarasov, I.A.; Lyashchenko, S.A. High uniaxial magnetic anisotropy of the $Fe_{1-x}Si_x$ films synthesized by MBE. *J. Magn. Magn. Mater.* **2017**, *440*, 161–163. [CrossRef]
52. Zakeri, K.; Barsukov, I.; Utochkina, N.K.; Römer, F.M.; Lindner, J.; Meckenstock, R.; von Hörsten, U.; Wende, H.; Keune, W.; Farle, M.; et al. Magnetic properties of epitaxial Fe_3Si/Mg(001) thin films. *Phys. Rev. B* **2007**, *76*, 214421. [CrossRef]
53. Ando, Y.; Hamaya, K.; Kasahara, K.; Ueda, K.; Nozaki, Y.; Sadoh, T.; Maeda, Y.; Matsuyama, K.; Miyao, M. Magnetic properties of epitaxially grown Fe_3Si/Ge(111) layers with atomically flat heterointerfaces. *J. Appl. Phys.* **2009**, *105*, 07B102. [CrossRef]
54. Komogortsev, S.V.; Varnakov, S.N.; Satsuk, S.A.; Yakovlev, I.A.; Ovchinnikov, S.G. Magnetic anisotropy in Fe films deposited on SiO_2/Si(001) and Si(001) substrates. *J. Magn. Magn. Mater.* **2014**, *351*, 104–108. [CrossRef]
55. Zhang, M.-L.; Ye, J.; Liu, R.; Mi, S.; Xie, Y.; Liu, H.-L.; Van Haesendonck, C.; Chen, Z.-Y. Study of magnetization reversal and anisotropy of single crystalline ultrathin Fe/MgO (001) film by magneto-optic Kerr effect. *Chin. Phys. B* **2016**, *25*, 047503. [CrossRef]
56. Liu, Y.C.; Chang, P.; Huang, S.Y.; Chang, L.J.; Lin, W.C.; Lee, S.F.; Hong, M.; Kwo, J. Magnetization reversal processes of epitaxial Fe_3Si films on GaAs(001). *J. Appl. Phys.* **2011**, *109*, 07D508. [CrossRef]
57. Lösche, A. N. F. MOTT, E. A. DAVIS. Electronic Processes in Non-Crystalline Materials Clarendon-Press, Oxford 1971 437 Seiten. £ 7,50. *Krist. Und Tech.* **1972**, *7*, K55–K56. [CrossRef]
58. Adkins, C.J. Conduction in granular metals-variable-range hopping in a Coulomb gap? *J. Phys. Condens. Matter* **1989**, *1*, 1253–1259. [CrossRef]
59. Sheng, P.; Abeles, B.; Arie, Y. Hopping Conductivity in Granular Metals. *Phys. Rev. Lett.* **1973**, *31*, 44–47. [CrossRef]
60. Kittle, C. *Introduction to Solid State Physics*; Willey: New Delhi, India, 2009; pp. 628–629, ISBN 978-0-471-41526-8.
61. Lee, P.A.; Ramakrishnan, T.V. Disordered electronic systems. *Rev. Mod. Phys.* **1985**, *57*, 287–337. [CrossRef]